Politecnico di Torino

Master's degree in Automotive Engineering

Academic year 2025/2026

Graduation session March 2026

Numerical development of a Predictive Combustion Model for an ICE running on hydrogen

Supervisors:
Prof. Federico Millo
Prof. Andrea Piano
Gianpaolo Quattrone, PhD

Graduating:
Riccardo Alberto Aleo, S320167

Table of contents

LIST OF FIGURES

LIST OF TABLES

0. Abstract

Hydrogen-fuelled internal combustion engines represent a promising solution for the decarbonization of road transport, benefiting from favourable combustion properties such as high flame speed and wide flammability limits, which enable high-efficiency engine operation and extended lean-burn capabilities. To support the development of hydrogen internal combustion engines while limiting experimental effort, numerical simulation represents a valuable tool for engine performance prediction, virtual calibration, and system-level analysis across a wide range of operating conditions, thus limiting extensive and costly experimental campaigns.

Within this framework, this thesis, made in collaboration with Westport Fuel Systems, focuses on the development of a complete 0D/1D model of a turbocharged hydrogen-fuelled internal combustion engine, developed in the commercially available software GT-SUITE.

The case study under investigation is a turbocharged PFI 3.5 L engine, originally designed for CNG operation and subsequently modified for hydrogen operation. The engine model includes a detailed representation of the full engine geometry, airpath system, and turbocharging components, and features a predictive combustion formulation specifically tailored to hydrogen applications.

An initial analysis of experimental data was carried out to highlight the main differences between hydrogen and CNG combustion, providing the basis for the adopted modelling and calibration strategy. The numerical model was then calibrated and validated against an extensive experimental dataset covering wide sweeps of engine load, boost pressure, air-fuel ratio, and spark timing. The validation activity demonstrated strong agreement between numerical predictions and experimental measurements in terms of in-cylinder pressure evolution and the main combustion-related indicators. The results show that the proposed modelling framework is capable of reliably predicting engine performance over a broad operating range. The developed model therefore represents an effective support tool for research and development activities related to hydrogen-fuelled internal combustion engines, enabling performance assessment and virtual calibration with reduced reliance on experimental testing.

1. Introduction

The current global landscape is characterized by a combination of environmental, economic, and political challenges that increasingly demand a profound transformation of existing energy systems. Among these challenges, climate change represents one of the most critical and urgent issues, driving governments, industries, and research institutions to pursue rapid and sustained reductions in greenhouse gas emissions. A growing body of scientific evidence has established a clear link between anthropogenic emissions and the rise in global average temperatures, with carbon dioxide (CO_2) identified as the primary contributor due to its long atmospheric lifetime and dominant share in total emissions.

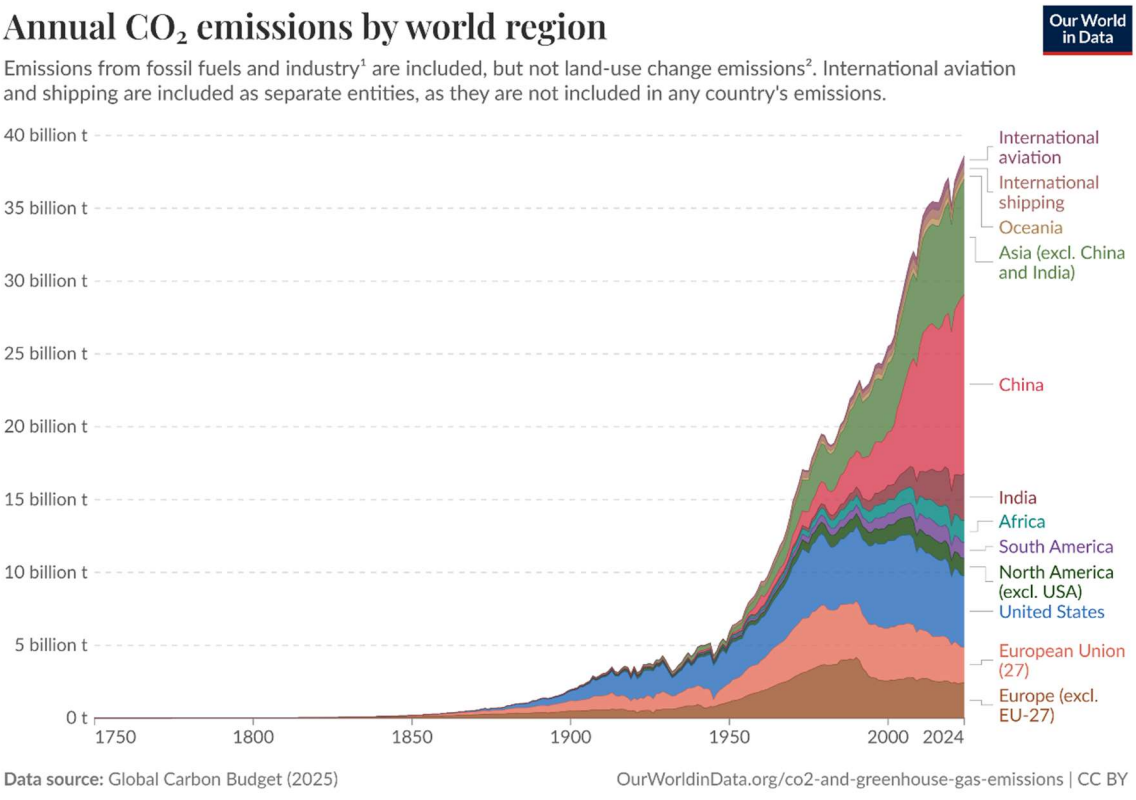

Figure 1: Annual global CO2 emissions by world region - Our World in Data

The increase in global CO_2 emissions is largely attributable to the extensive use of fossil fuels to satisfy rising energy demand. Emissions from fossil fuel combustion have increased steadily over recent decades, while emissions related to land use change, such as deforestation, have shown a comparatively modest decline. This imbalance has intensified the greenhouse effect, contributing to global warming and to increasingly evident consequences, including extreme weather events, accelerated glacier melting, and rising sea levels. These phenomena have direct environmental, economic, and social impacts, reinforcing the urgency of effective mitigation strategies.

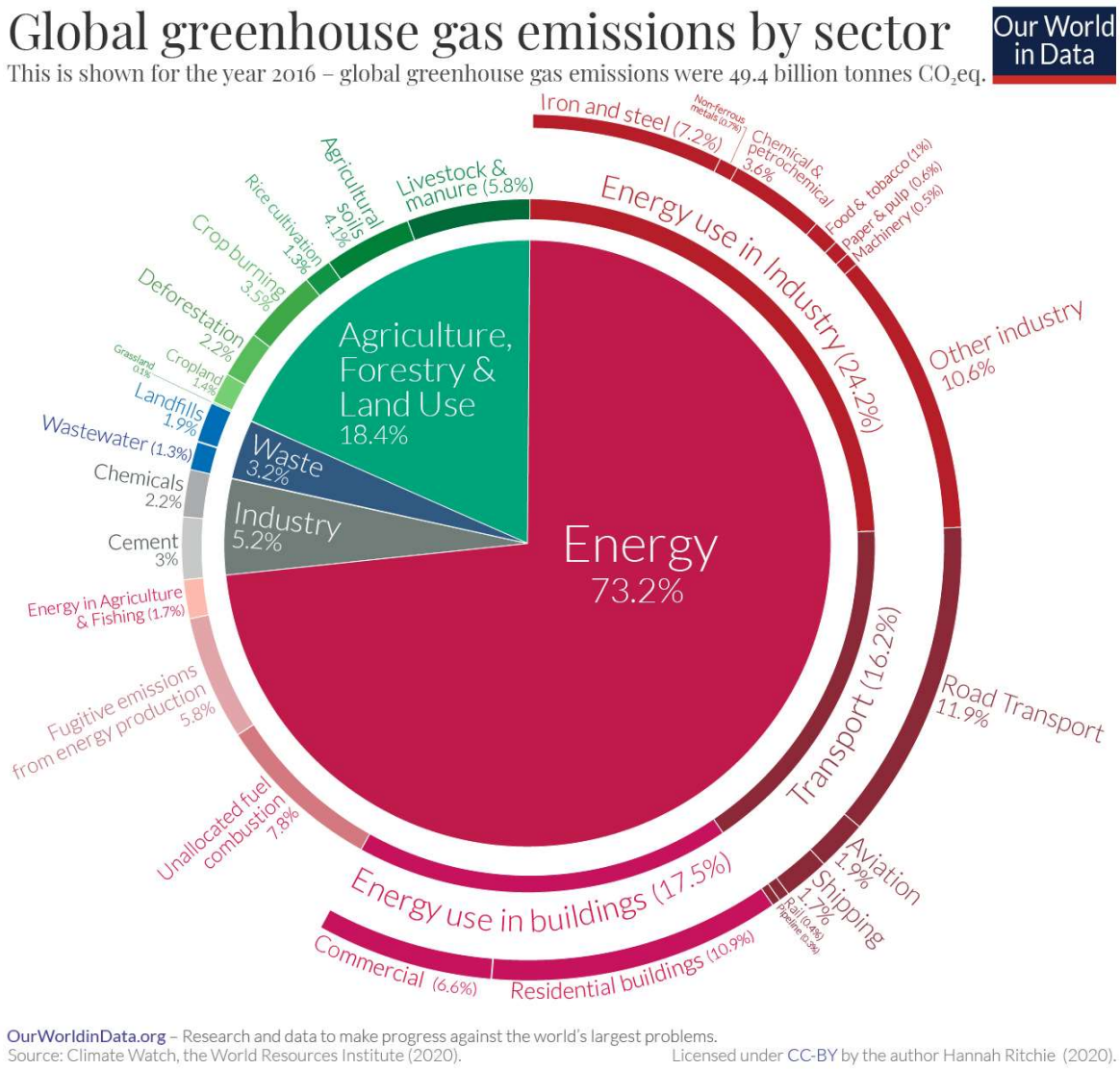

Figure 2: Influence in the total CO2 emissions of each sector - Our World in Data

In response, international agreements and regulatory frameworks have been established to coordinate emission reduction efforts and promote sustainable development. Within Europe, the Green Deal and the Emissions Trading System (ETS) play a central role in

promoting energy efficiency and the deployment of low-emission technologies. These initiatives are aligned with the United Nations Sustainable Development Goals, particularly SDG 7 on affordable and clean energy and SDG 13 on climate action and define a structured pathway toward sustainable economic growth. Nevertheless, the energy transition also involves significant social and economic challenges, particularly in regions historically dependent on fossil fuel–based industries, where infrastructure decommissioning and industrial restructuring may lead to socio-economic disruptions.

Within this broader framework, the transportation sector represents one of the most critical areas for intervention. Transport accounts for approximately 25% of global CO_2 emissions from energy-related sources, with road transport being the dominant contributor. As a result, the sector has become a focal point of regulatory action. The European Union, currently the third-largest contributor to transport-related CO_2 emissions after the United States and China, has introduced a regulation requiring a 100% reduction in CO_2 emissions from new vehicles by 2035. This measure, announced in 2023, effectively mandates that all newly registered passenger cars be zero-emission by that date. However, the ambitious nature of this target has raised concerns regarding industrial competitiveness, employment impacts, and technological readiness, particularly in countries with strong automotive sectors such as Italy and Germany, leading to a planned legislative review in 2026.

Similar decarbonization efforts are underway globally. In the United States, the Environmental Protection Agency has outlined a roadmap toward a zero-emissions future, while China continues to promote New Energy Vehicles through extensive incentive programs. Despite differences in regulatory approaches, these initiatives converge toward a common objective: reducing transport-related emissions in line with the Net Zero Emissions by 2050 (NZE) scenario.

To achieve these objectives, original equipment manufacturers are pursuing multiple technological pathways. Battery electric vehicles (BEVs) currently represent the most mature alternative to conventional internal combustion engines, offering high energy efficiency and zero tailpipe emissions. However, from a life-cycle assessment perspective, their effectiveness in reducing CO_2 emissions depends strongly on the carbon intensity of the electricity mix. Moreover, BEVs are characterized by high upfront costs, long recharging times, and the need for large battery capacities, which limit their applicability in heavy-duty transport where vehicle mass, payload, and operational flexibility are critical.

Fuel cell electric vehicles (FCEVs) address some of these limitations by enabling fast refueling and offering higher gravimetric energy density than batteries. Fuel cells typically achieve high efficiency, particularly under partial to moderate load conditions. Nevertheless, their widespread deployment is currently constrained by the limited availability of hydrogen refueling infrastructure and the relatively low technological maturity of fuel cell systems, resulting in high costs and limited economies of scale.

An alternative strategy focuses on modifying the fuel rather than the powertrain architecture, thereby allowing continued use of internal combustion engines. Biofuels offer partial carbon neutrality but are constrained by sustainability concerns related to land use

and food competition. Electrofuels, synthesized from renewable hydrogen and captured CO_2, are compatible with existing engines but are significantly limited by low energy conversion efficiency. Depending on the application, electricity-to-useful-energy conversion efficiencies for e-fuels range from approximately 10% to 35%, implying renewable electricity requirements that are two to fourteen times higher than those of direct electrification solutions.

Within this context, hydrogen-fueled internal combustion engines (H_2-ICEs) have emerged as a promising alternative. Compared to BEVs, H_2-ICEs offer extended driving range and refueling times comparable to conventional vehicles. Hydrogen also exhibits a significantly higher gravimetric energy density than batteries, resulting in more favorable vehicle mass characteristics, particularly for heavy-duty applications. Unlike FCEVs, H_2-ICEs can be developed by adapting existing internal combustion engine platforms, allowing reuse of established manufacturing processes, infrastructure, and supply chains. Furthermore, hydrogen engines can operate with lower hydrogen purity than fuel cells, enhancing their robustness during early stages of hydrogen market deployment.

The environmental performance of hydrogen-based combustion technologies must be evaluated through a life-cycle assessment approach, with hydrogen production playing a central role. Hydrogen is commonly classified according to production pathways using a color-based nomenclature. Gray hydrogen, produced via methane reforming without carbon capture, remains the most widespread but is associated with high CO_2 emissions. Blue hydrogen incorporates carbon capture and storage, while green hydrogen is produced via water electrolysis using renewable electricity and represents the only pathway compatible with deep decarbonization. According to the Global Hydrogen Review 2024, electrolysis currently accounts for approximately 4% of global hydrogen production, with projections indicating a potential increase to around 22% by 2050. Current green hydrogen production costs are estimated at 4–6 USD/kg, with expected reductions of 30–50% by 2030, potentially reaching 2–3 USD/kg.

From a thermodynamic and combustion standpoint, hydrogen exhibits several properties that make it attractive for internal combustion engines. Hydrogen contains no carbon, eliminating carbon-based emissions such as CO_2, CO, and soot during combustion, while nitrogen oxides (NO_x) remain the primary regulated pollutants. Hydrogen has a high lower heating value of approximately 120 MJ/kg, nearly three times that of gasoline or diesel on a mass basis. Its high diffusion coefficient promotes rapid air–fuel mixing, which is particularly advantageous in direct injection configurations.

Hydrogen also exhibits a laminar flame speed approximately four to five times higher than that of gasoline at stoichiometric conditions, remaining relatively high even under lean mixtures. These characteristics enable lean combustion strategies that can reduce throttling losses and peak combustion temperatures, improving thermal efficiency and mitigating NO_x formation. However, hydrogen combustion also presents challenges related to abnormal combustion phenomena. Despite hydrogen's high autoignition temperature, its extremely low minimum ignition energy significantly increases the risk of pre-ignition and backfiring, particularly in premixed combustion strategies. The low quenching distance

of hydrogen–air mixtures further increases heat transfer losses and the likelihood of surface-induced ignition.

Hydrogen storage represents an additional critical challenge. At atmospheric pressure and a temperature of 273 K, hydrogen density is approximately one order of magnitude lower than that of natural gas, resulting in very low volumetric energy density. To overcome this limitation, hydrogen is typically stored at high pressures. At 350 bar and 273 K, hydrogen density reaches approximately 31 kg/m³, while current automotive storage systems commonly operate at pressures up to 700 bar. Even under these conditions, the volumetric energy density of compressed hydrogen remains approximately 7–8 times lower than that of gasoline or diesel, although it is about three times higher than that of lithium-ion batteries.

The use of high-pressure hydrogen introduces additional safety and material challenges. Hydrogen embrittlement can compromise the mechanical integrity of metallic components exposed to high-pressure hydrogen environments, while hydrogen's high diffusivity increases the risk of leakage. Consequently, dedicated design solutions are required for both vehicle systems and refueling infrastructure, including material selection, sealing technologies, and safety protocols.

Overall, hydrogen internal combustion engines represent a technically viable and potentially cost-effective pathway for transport decarbonization, particularly in applications where fast refueling, long range, and high energy density are critical. Their successful deployment depends on advances in combustion control, high-pressure storage technologies, and the availability of low-carbon hydrogen, positioning H_2-ICEs as a complementary solution within a diversified and resilient low-emission transport strategy.

The automotive R&D is currently investing a remarkable effort into the electrification of the powertrain, to address the issue of air pollution and global warming. During the last decades, the problem of the worldwide increase of the average temperature – with the associated catastrophic consequences for our planet – has been taken more and more seriously in any sector relative to production and mobility.

Although the transports sector is not the biggest contributor to CO_2 emissions, still it provides nearly the 16% of the total emitted CO_2, and 75% of this comes from road transport. Therefore, a green revolution had to be started in the mobility as well. However, considering a single technology for supplying power to the vehicles is not feasible, due to the nature of the current processes to produce energy. This leads the companies to identify which technologies suit each class of vehicle the most. In this sense, relying on already well consolidated technologies - like internal combustion engines – is a valid solution, especially if carbon-free fuels are employed (e.g. hydrogen).

Exploiting also the data shown in Figure 3, compared to the common carbon fuels, hydrogen shows the following characteristics:

Property	Unit	Gasoline	Methane	Hydrogen
Density[1]	[kg/m^3]	~ 760	0.68	0.09
Stoichiometric Air Demand	[kg_A/kg_F]	14.0	17.2	34.3
Lower Heating Value	[MJ/kg]	42.5	50	120
Minimum Ignition Energy[2]	[mJ]	0.24	0.29	0.017
Ignition limits λ-range	[-]	0.4 – 1.4	0.6 - 2	0.13 - 10
Laminar Flame Speed[3]	[cm/s]	~ 40	~ 42	~ 230

[1] Ambient conditions, [2] Ambient conditions and λ=1, [3] Ambient conditions and λ=1.4÷1.7

Source: Verhelst, S., Wallner, T., "Hydrogen-fueled internal combustion engines," Progress in Energy and Combustion Science, 35:6, 2009

Figure 3: Comparison of the properties between Hydrogen, Gasoline and Methane

The advantages are clear:

- No carbon emissions (CO, HC, PM), net of those coming from the cavitation of lubricant oil for cylinder lubrication and for the valves guide.
- Wide flammability range (4-76%): this translates into the chance of running the engine extremely lean, especially at part load, without occurrence of misfire. This translates in a better thermal efficiency of the combustion process (see Figure 4)
- High flame laminar speed: compared to the common fuels, hydrogen shows a larger burning speed (about 1.85 m/s against the other fuels that barely reach 1 m/s). This translates into the chance of having a practically iso-choric combustion, thus resembling an ideal combustion process.
- High Q_{LHV}/α_{st} ratio (3.47 against 3 for gasoline): a stoichiometric mixture of hydrogen will develop about 14% more power than a stoichiometric mixture of gasoline. In other words, hydrogen allows to reach higher combustion efficiency
- High Research Octane Number (RON): $RON_{H2} \approx 130 > RON_{gasoline} \approx 95$, i.e. hydrogen results to be more resistant to knock, thus allowing to consider higher compression ratios than those of typical gasoline engines.

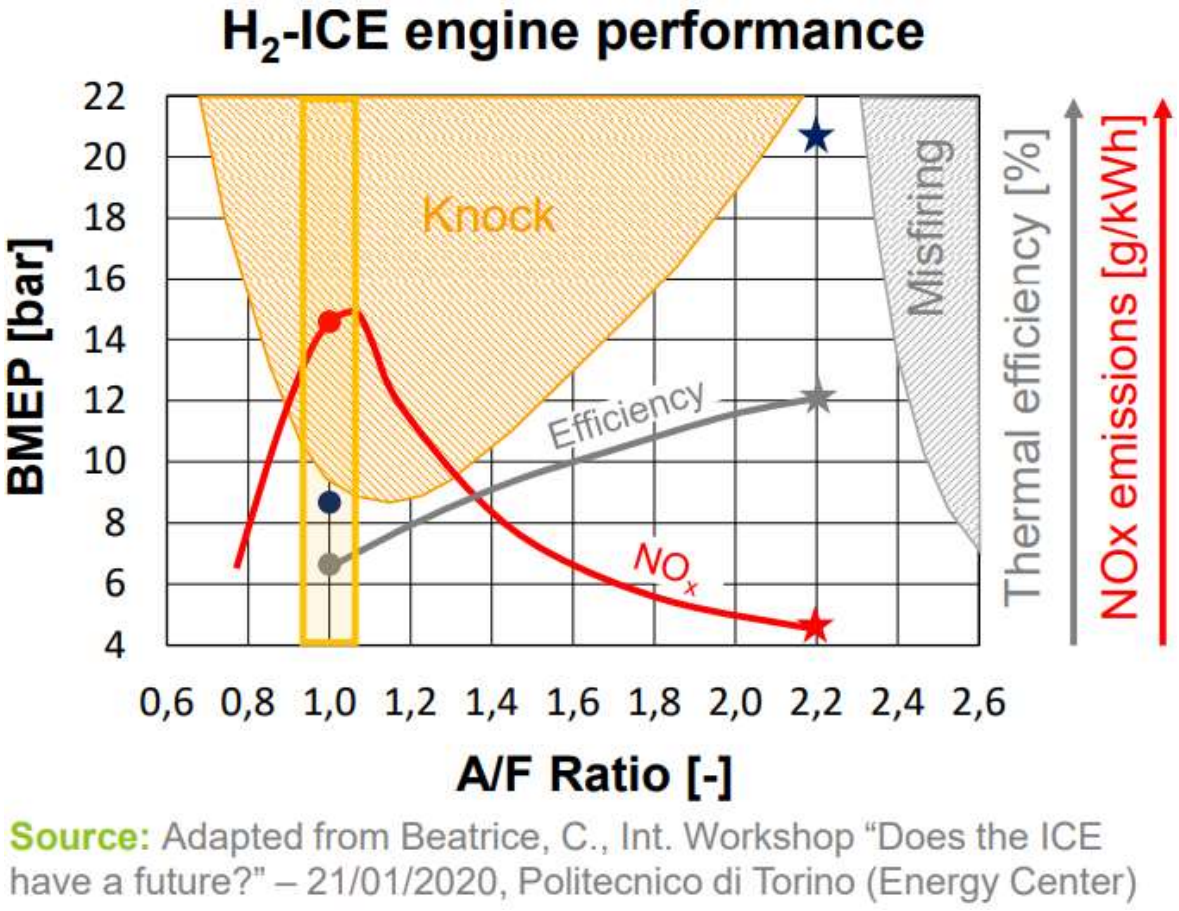

Figure 4: Engine performance window exploitable by Hydrogen ICEs

Unfortunately, these pros come with some drawbacks:

- Concrete risk of backfire into the intake manifold or pre-ignition inside the combustion chamber, due to the low activation energy of this fuel (about 0.02 mJ). This is true especially for PFI engines, that is the case under study
- Lower volumetric efficiency, if compared to petrol-based fuels, due to the gaseous state of aggregation of hydrogen, at ambient conditions.
- Possible embrittlement of the material of the tank, due to the high reactivity to high-pressure hydrogen
- Significant difference between Research Octane Number (≈130) and Motor Octane Number (≈65), therefore it is likely to have remarkable discrepancy between the testing conditions of the only fuel at the Rapid Compression Machine and the actual application to a real engine

That of heavy-duty vehicles for goods transport is one of the sectors that are more sensitive to the technological progress in power supply. The more the vehicles are technologically

updated, the higher their efficiency becomes, the lower the cost per unit travelled distance. Yet, a continuous complete renewal of heavy-duty vehicles is unsustainable for any company. This is why the conversion of the fuel supply system of an already existing vehicle can be considered a valid trade-off between cost and benefit.

One of the main challenges in this sense is to ensure a high-performance product, while minimising the cost of real-life tests. This is why a so-called “digital twin” of the engine is essential. Such a tool allows potentially infinite modifications and tests achievable in short time and with basically no cost, through the development of a numerical thermo-fluid-dynamic model. The aim of these latter is to resemble the behaviour of its real counterpart as accurately as possible. Nevertheless, a punctual prediction cannot be reached due to numerical errors and since mathematical models cannot fully represent the extremely complex nature of the processes that occur inside such a system like an internal combustion engine.

This said, the scope of this thesis is to provide a methodology for the simulation of an engine running on hydrogen and for the subsequent development and calibration of a predictive model, to support the experimental activity at the test bench with a reliable tool that allows to optimize cost and time for a company.

2. Case study and methodology

2.1 Case study

This project is realised around a turbocharged port fuel injection 3500 cm^3 engine and during this thesis it will be analysed throughout the whole contour plane, in terms of load and speed. Table 1 shows the main specifics of the engine:

Case study	
Bore [mm]	96
Stroke [mm]	122
Conn Rod Length [mm]	190.5
Nominal Compression Ratio	12
Peak Power	95 kW @ 2400 RPM
Peak Torque	460 Nm @ 1200 RPM

Table 1: Specifics of the Case study

At the test bench, the engine is instrumented with thermocouples and pressure sensors connected to the electronic control unit (ECU), which manages both test control and data acquisition. Figure 5 shows an overview of the system of cables and sensors that surrounds the head of the engine.

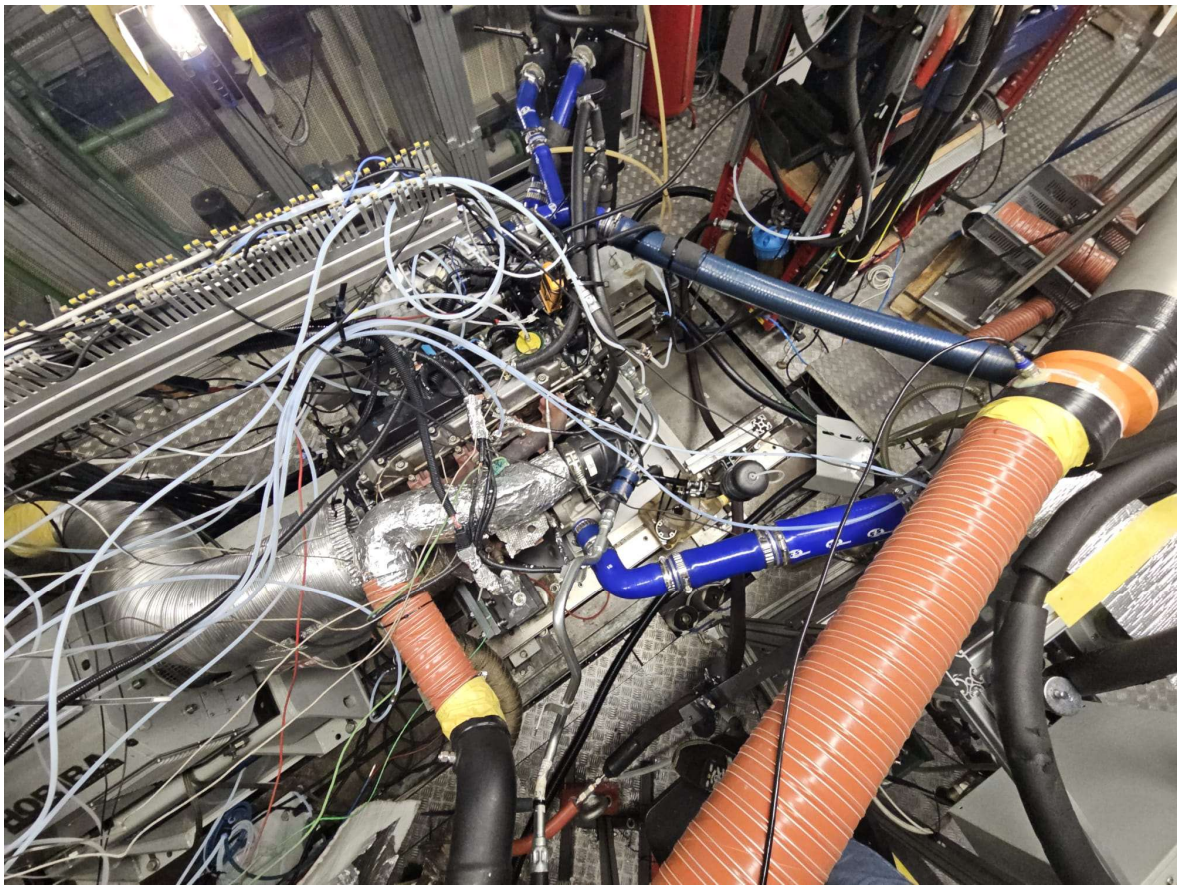

Figure 5: General overview of the test bench object of the analysis presented in this thesis

Intake air enters the system through a Venturi device and flows toward the compressor, following a defined path along which the main thermodynamic conditions are monitored. The experimental campaign was conducted without an Exhaust Gas Recirculation (EGR) system. Although the installation of an aftertreatment system at the tailpipe was possible, it was not implemented in order to avoid the introduction of additional backpressure that could influence the experimental results. Furthermore, the presence of an aftertreatment system was not considered critical with respect to the objectives of this thesis, that focuses on the only performance of the engine subsystem.

2.2 Methodology

Before entering the details of any conduced analysis, the methodology that was considered across the project is worth of being clarified. Figure 6 can be employed as a support for this argumentation.

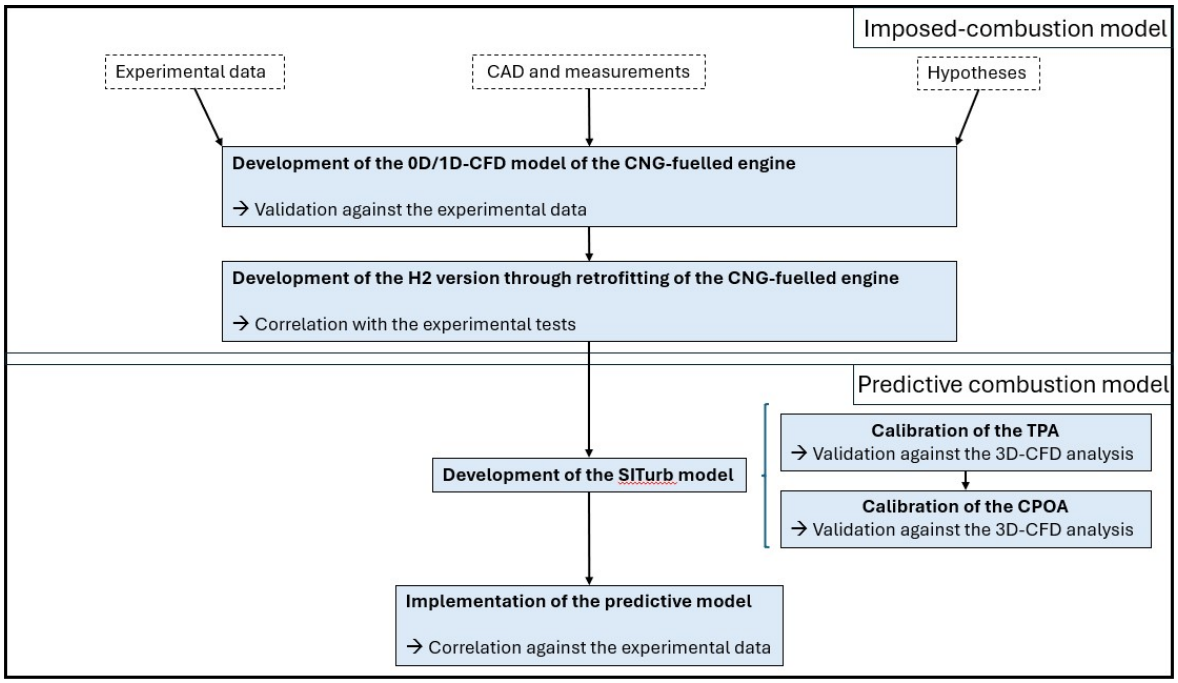

Figure 6: Graphical representation of the methodology that was followed throughout the thesis

Starting from the provided data – i.e., the experimental data recorded at the test bench, the CAD and the in-situ measurements – and the hypotheses that were taken into account – and that will be better explained in the relevant chapters along the thesis -, the imposed-combustion model fuelled with CNG was built and correlated with the experimental dataset. This passage was done so to exploit the fact that the CNG engine underwent more complete tests, for instance, information across the whole contour plan of the engine were available. Once the correlation was completed, the model running on H2 was realised through retrofitting and validated against the data retrieved at the test bench. The tests on hydrogen focused mainly on the sweeps of air-to-fuel-ratio, therefore starting directly from this fuel would have led to a less solid model from this analysis could have start from. The subsequent successful correlation of the model running on hydrogen with the experimental results will then pave the way for the calibration of the predictive SITurb model. First, a Three Pressure Analysis (TPA) will be assessed for predicting the turbulent phenomena, taking as reference for the calibration the results obtained by the provided 3D-CFD analysis and employing the Genetic Algorithm for the optimization of the parameters that influence

the equations of turbulence. Then, the predictive combustion model will be developed through a Cylinder Pressure Oscillation Analysis (CPOA), in which the parameters involved in the equation governing the laminar speed and the turbulent speed of the flame front will be optimized – following the same procedure as in the TPA – and validated against the experimental pressure cycles and burn rates. Considering the provided dataset, part of it will be employed for the calibration of the combustion object. Once the calibration will be accomplished, the rest of the provided dataset will be exploited for the validation of the SITurb, i.e., for the evaluation of its predictive capabilities. Eventually, the obtained SITurb model will be set inside the complete model for the correlation between the performance that were recorded at the test bench and the performance predicted by the 0D/1D-CFD model.

3. Experimental data analysis

An accurate and systematic evaluation of the experimental data is essential to properly interpret the effects of engine calibration on combustion behaviour and overall performance. The objective of the present analysis is to investigate how the selected calibration parameters interact with each other across different operating conditions during the experimental tests. Particular attention is devoted to the identification of combined effects rather than isolated trends, in order to provide a consistent interpretation of the observed phenomena.

The main swept calibration parameters considered in this study are boost pressure, spark advance, and air-to-fuel ratio (λ). Table 2 summarizes the sweeps that were employed during the experimental tests.

Parameter	Sweep
Rotational speed [rpm]	1400÷2200
Air-to-fuel ratio (λ) [-]	1.8÷3.4
Spark advance [deg bTDC]	-5÷35
Boost pressure [kPa]	160÷200

Table 2: Overview of the swept calibration parameters

These parameters were varied according to predefined test matrices. Although spark advance is one of the experimentally controlled variables, it will not be explicitly discussed in most cases. Instead, the analysis primarily relies on the combustion phasing parameter MFB50, defined as the crank angle at which 50% of the injected fuel mass is burned. This choice is motivated by the fact that MFB50 is more representative of the combustion process and allows a direct comparison between operating points characterized by different ignition timings. Moreover, variations in MFB50 can be directly associated with spark advance or retard effects, enabling a clearer interpretation of combustion trends.

Some graphs will also report results in terms of NOx emissions; however, this aspect is considered only for the sake of completeness, since no EGR sweep was performed during the experimental campaign. Nevertheless, it is worth at least mentioning noxious emissions, as they are always discussed when dealing with hydrogen combustion.

Furthermore, except for brake torque when explicitly required, the quantities presented in this chapter are indicated values. The main reason lies on the fact that they are more relevant to the focus of this analysis, i.e., the in-cylinder combustion phenomenon, and indicated quantities are not affected by mechanical efficiency, which is physically dominated by non-linear trends across the engine speed range.

Before presenting and discussing the experimental results, it is important to clarify that although four different operating regimes were investigated during the experimental tests, only those that clearly highlight the phenomena of interest are presented in this thesis. Moreover, no significant qualitative differences were observed among the tested engine speed regimes with respect to the analysed aspects. For this reason, the discussion is limited to 1400 rpm, without any loss of generality in the interpretation of the results.

A smooth introduction to the experimental data analysis can be accomplished by presenting the torque vs MFB50 diagram. Figure 7 shows the effect of the sweep of MFB50 on the torque at 1400 rpm, at a boost pressure of 1.6 bar.

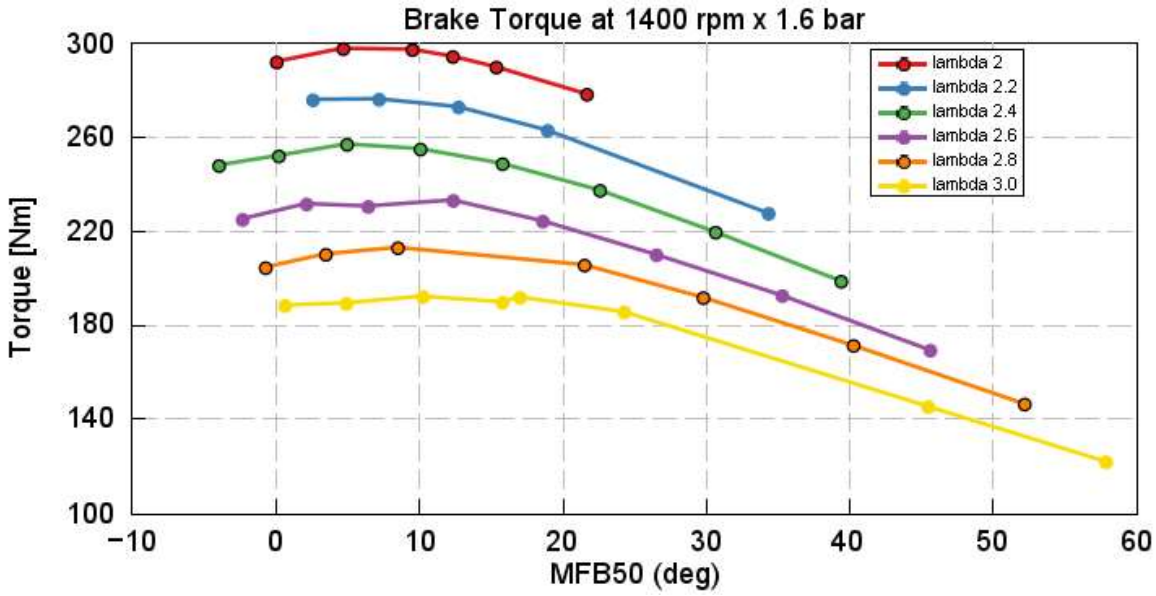

Figure 7: Brake Torque curves vs MFB50 at 1400 rpm, 1.6 bar of boost pressure, for different air-to-fuel ratios

Higher values of MFB50 indicate that the barycentre of the combustion process is shifted further away from Top Dead Centre (TDC), typically suggesting a retarded spark timing, at least for a constant charge composition. At a fixed air-to-fuel ratio, a clear peak corresponding to the Maximum Brake Torque (MBT) condition can be observed. As a preliminary remark, the MBT timing is reached at approximately 2–4 crank angle degrees after TDC, in contrast with the well-known 8–10 CA aTDC, typical of gasoline and Diesel engines. This behavior reflects the higher combustion speed of hydrogen compared to conventional fossil fuels. Before and after the MBT point, torque progressively decreases due to different mechanisms: in the case of advanced ignition, an increase in pumping work occurs, while in the case of retarded ignition, the expansion stroke is not fully exploited. On the other hand, when a fixed MFB50 is considered, it is evident that leaner mixtures lead to a reduction in output torque. This behaviour is also associated with the decrease in exhaust gas temperature as the mixture becomes leaner, which in turn reduces the available enthalpy at the turbine inlet. As the air-to-fuel ratio increases, the wastegate valve closes earlier, preventing the achievement of the boost target compared to richer mixtures. Under these conditions, the capability of hydrogen to operate at air-to-fuel ratios higher

than those achievable with fossil fuels does not provide an advantage in terms of torque output.

However, the main benefit of hydrogen operation emerges in terms of thermal efficiency. Figure 8 and Figure 9 support the observations that are going to be done.

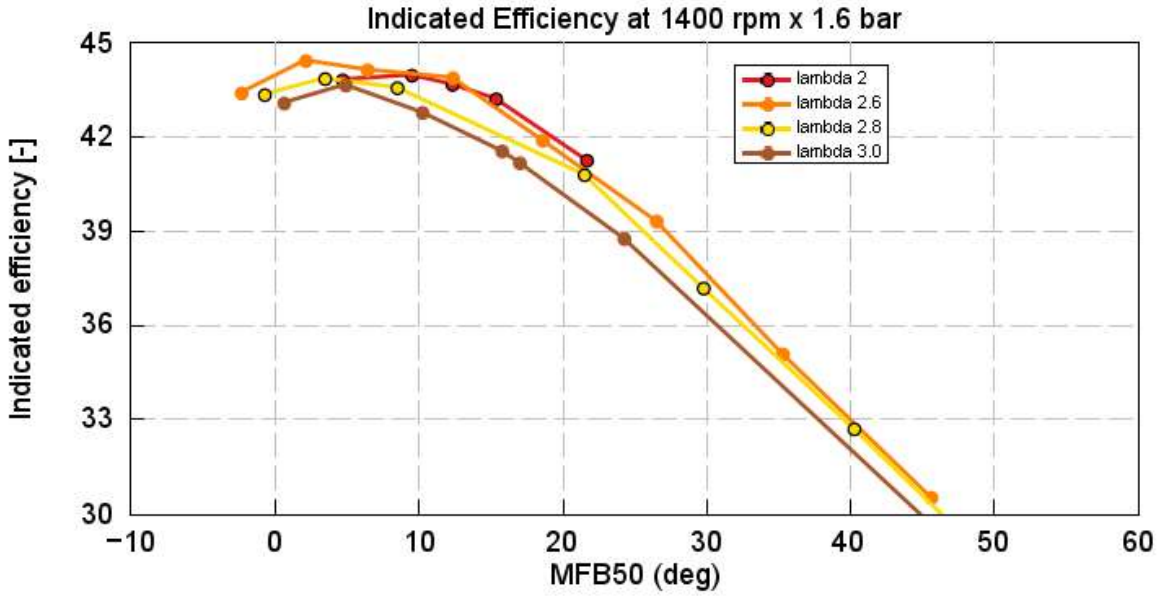

Figure 8: Indicated Efficiency curves vs MFB50 at 1400 rpm, 1.6 bar of boost pressure, for different air-to-fuel ratio

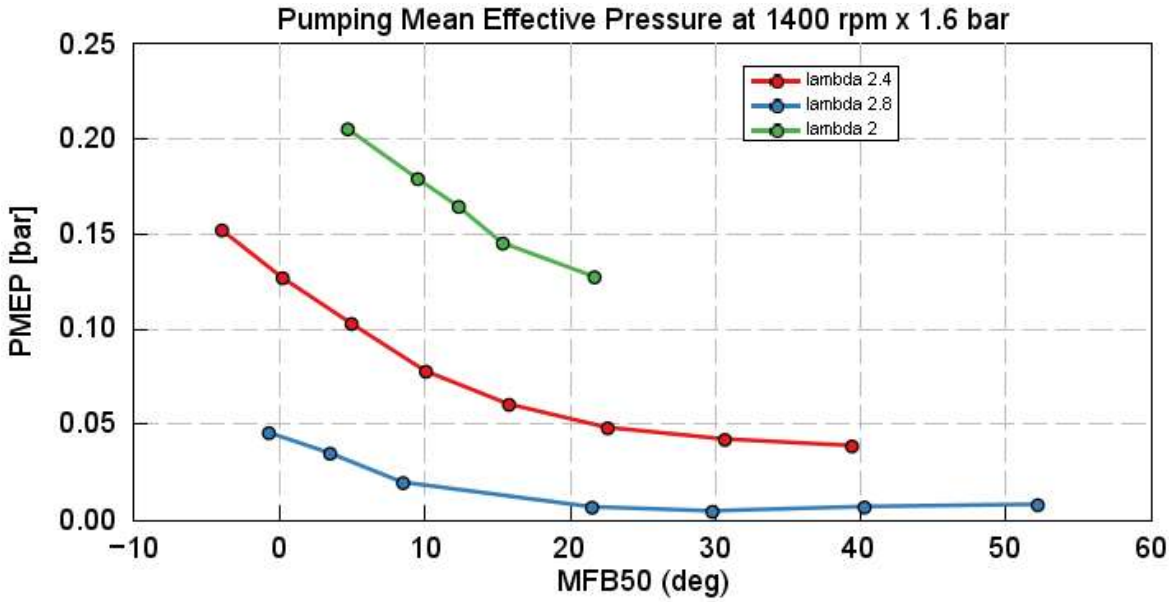

Figure 9: PMEP curves vs MFB50 at 1400 rpm, 1.6 bar of boost pressure, for different air-to-fuel ratios

The indicated thermal efficiency benefits from reduced heat transfer between the gas and the cylinder walls. At the same time, a progressive increase in Pumping Mean Effective

Pressure (PMEP) can be observed. More precisely, the typical advantage of turbocharged engines in achieving a positive pumping loop is gradually weakened as the mixture becomes leaner, eventually approaching zero. Beyond a certain air-to-fuel ratio threshold, the increase in PMEP dominates over the reduction in heat transfer, resulting in an overall decrease in efficiency.

Figure 10 and Figure 11 provide an overview on the trends followed by the thermodynamic conditions at the inlet of the turbine.

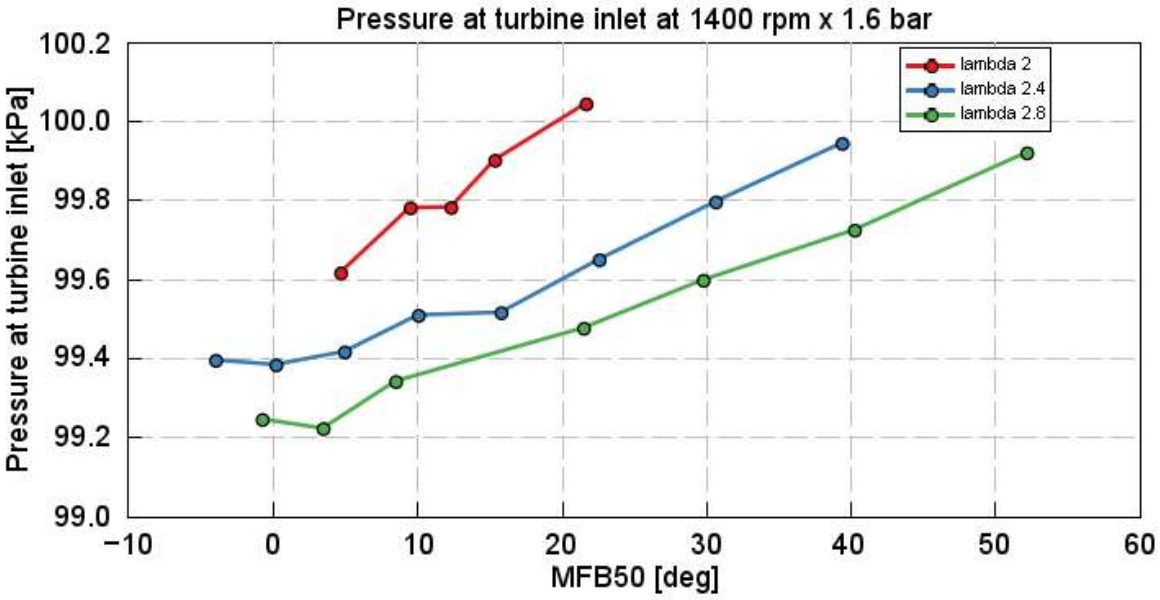

Figure 10: Pressure at turbine inlet curves vs MFB50 at 1400 rpm, 1.6 bar of boost pressure, for different air-to-fuel ratios

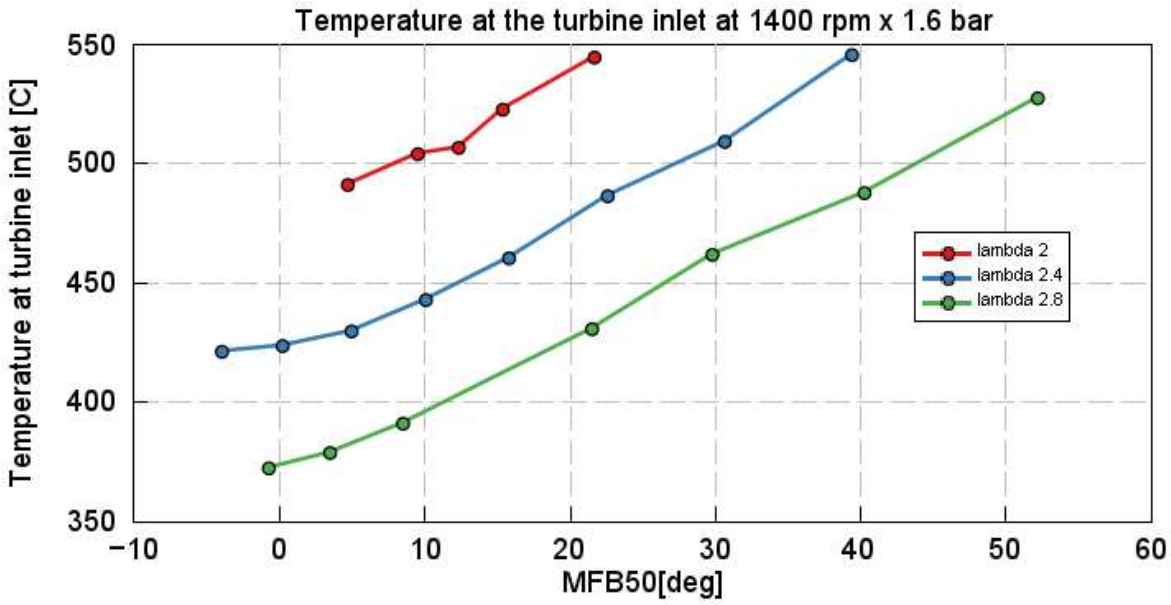

Figure 11: Temperature at turbine inlet curves vs MFB50 at 1400 rpm, 1.6 bar of boost pressure, for different air-to-fuel ratios

Emphasizing the effects of calibration parameter sweeps on this stage is crucial, as these conditions strongly influence overall engine performance. Both pressure and temperature at the turbine inlet exhibit similar trends as a function of MFB50 for different air-to-fuel ratios. In general, retarding combustion results in less energy being converted into useful work within the cylinder; consequently, a larger fraction of energy remains in the form of heat and is discharged into the exhaust system, explaining the observed trends. Conversely, increasing the air-to-fuel ratio reduces the thermodynamic levels at the turbine inlet, due to the lower amount of fuel burned and, therefore, lower released energy.

In parallel, the analysis of noxious emissions provides additional insight. Figure 12 presents representative NO_x trends.

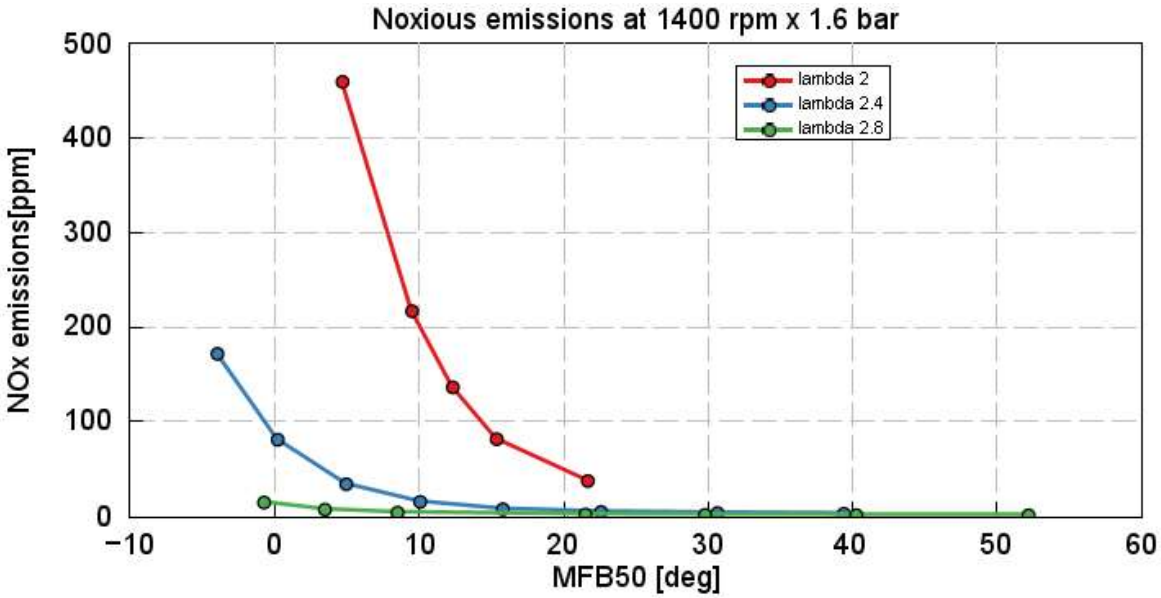

Figure 12: Noxious emission curves vs MFB50 at 1400 rpm, 1.6 bar of boost pressure, for different air-to-fuel ratios

NO_x formation can be explained through the Zeldovich mechanism, according to which the main reactions involved are:

$$N + O_2 \leftrightarrow NO + O$$

$$N_2 + O \leftrightarrow NO + N$$

These reactions are characterized by high activation energies and typically occur in oxygen-rich environments, such as the lean operating conditions analysed in this thesis. In particular, they require temperatures above approximately 1850 K and sufficient residence time of the gases within the combustion chamber. As discussed above, both conditions are met at low values of MFB50 and λ, corresponding to combustion close to MBT timing and relatively richer mixtures. As combustion is progressively retarded, in-cylinder temperatures decrease and combustion occurs closer to the Exhaust Valve Opening (EVO), assuming unchanged valve phasing, thereby reducing or even suppressing NOx formation. In the absence of EGR, as in this case study, a trade-off between performance and emissions is unavoidable and must be addressed considering the characteristics and capabilities of the aftertreatment system. As shown in the graph, the benefit of combustion retard in reducing NOx emissions is more pronounced for richer mixtures and follows an exponential-like trend. Beyond a certain point, further combustion retard results in marginal NOx reduction while causing a significant deterioration in efficiency and performance.

Since up to this point the air-to-fuel ratios that were taken into account are extremely lean, and given nature of spark-ignition engines, pointing out what happens in terms of stability of the combustion process is relevant for the scope of this thesis. The observed data do not need a long analysis, however Figure 13 provides an interesting focus in this sense.

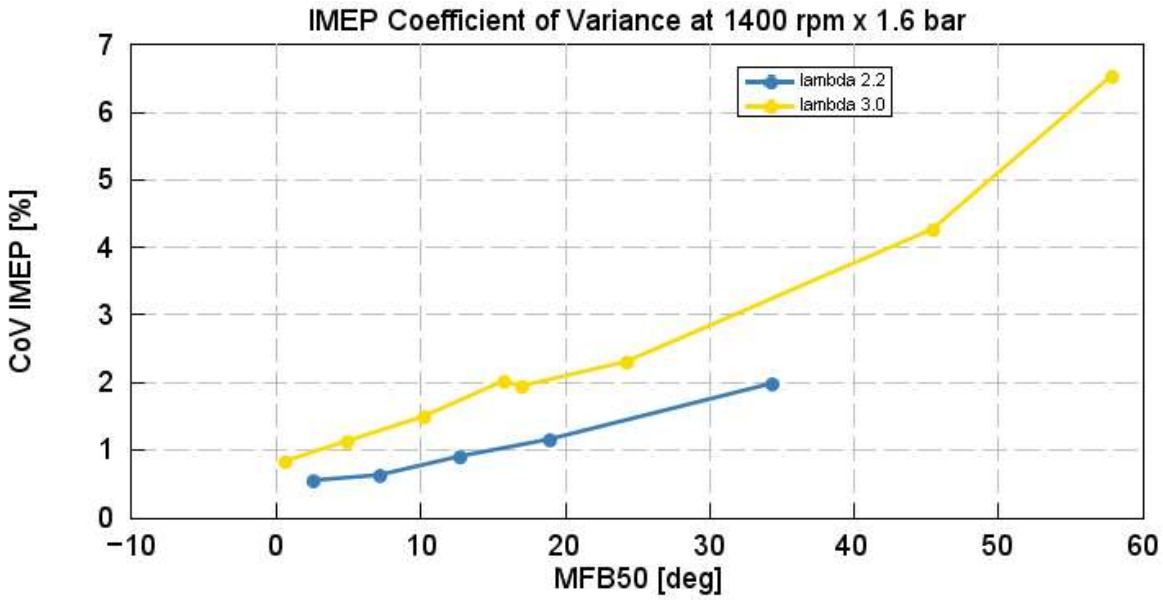

Figure 13: Coefficient of Varaince of the IMEP curves vs MFB50 at 1400 rpm, 1.6 bar of boost pressure, for different air-to-fuel ratios

The presented graph shows what happens to the Coefficient of Variance of the IMEP (CoV_{IMEP}) while the MFB50 increases. The CoV of IMEP is defined as:

$$CoV_{IMEP} = \frac{\sigma_{IMEP}}{IMEP} \times 100$$

where σ_{IMEP} is the standard deviation of the average IMEP (taking typically the ensemble average among 100 consecutive cycles). As a general guideline, the CoV_{IMEP} should not exceed 3-5%. As shown in Figure 13 (same as previous), this threshold is reached at relatively moderate combustion retard only in the case of extremely lean mixtures. For sake of completeness, isolated cases of knock were detected; however, these events occurred only under specific engine phasing conditions and were intentionally explored to assess the operational limits of the engine.

As a final remark, Figure 14 shows the influence of the boost pressure level, rather than another, on the indicated efficiency.

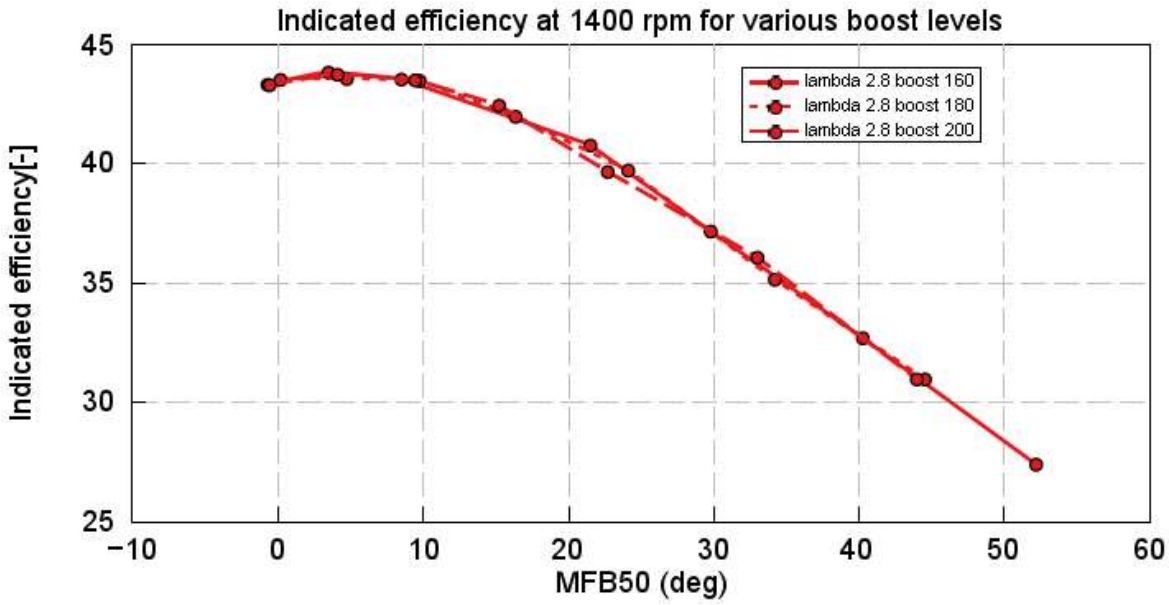

Figure 14: Indicated efficiency curves vs MFB50 at 1400 rpm, at an air-to fuel ratio of 2.8, for different boost pressures

For the same rotational speed regime, the analysis does not loose generality, in terms of thermal efficiency, that is one of the key-points of this analysis, as debated above. This occurs because the choice of the boost directly influences the output torque quantitatively, nevertheless, it does not constitute a discriminant factor inside the dynamics of the heat exchange, because clearly, for a same MFB50, when the boost increases, the extracted work grows proportionally with the growth of the introduced heat.

4. Development of the 1D-CFD model

4.1 Geometrical construction of the model

Basing on the available starting data that were mentioned in chapter 2, the construction of the 1D-CFD model needed precise strategy and methodology, in order to be accomplished. The methodology in this sense was, macroscopically:

1. Setup of all the available experimental data (geometrical, thermo-fluid dynamic, controls)
2. Optimization of the geometry through the tools provided by GT-Power (where possible)
3. Proper estimation of missing data through indirect measurements and critic sense

Figure 15 shows an overview of the obtained model.

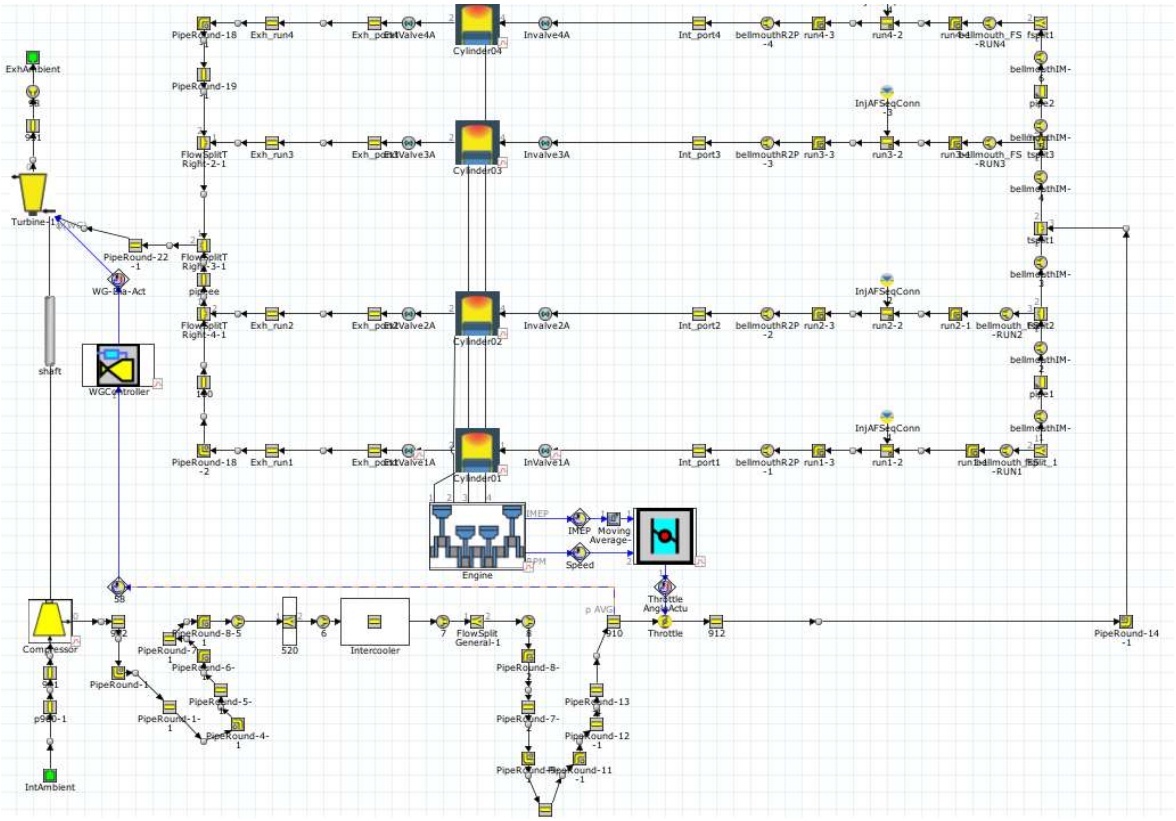

Figure 15: Overview of the 0D/1D-CFD model

It is possible to identify three areas, each built following a different approach:

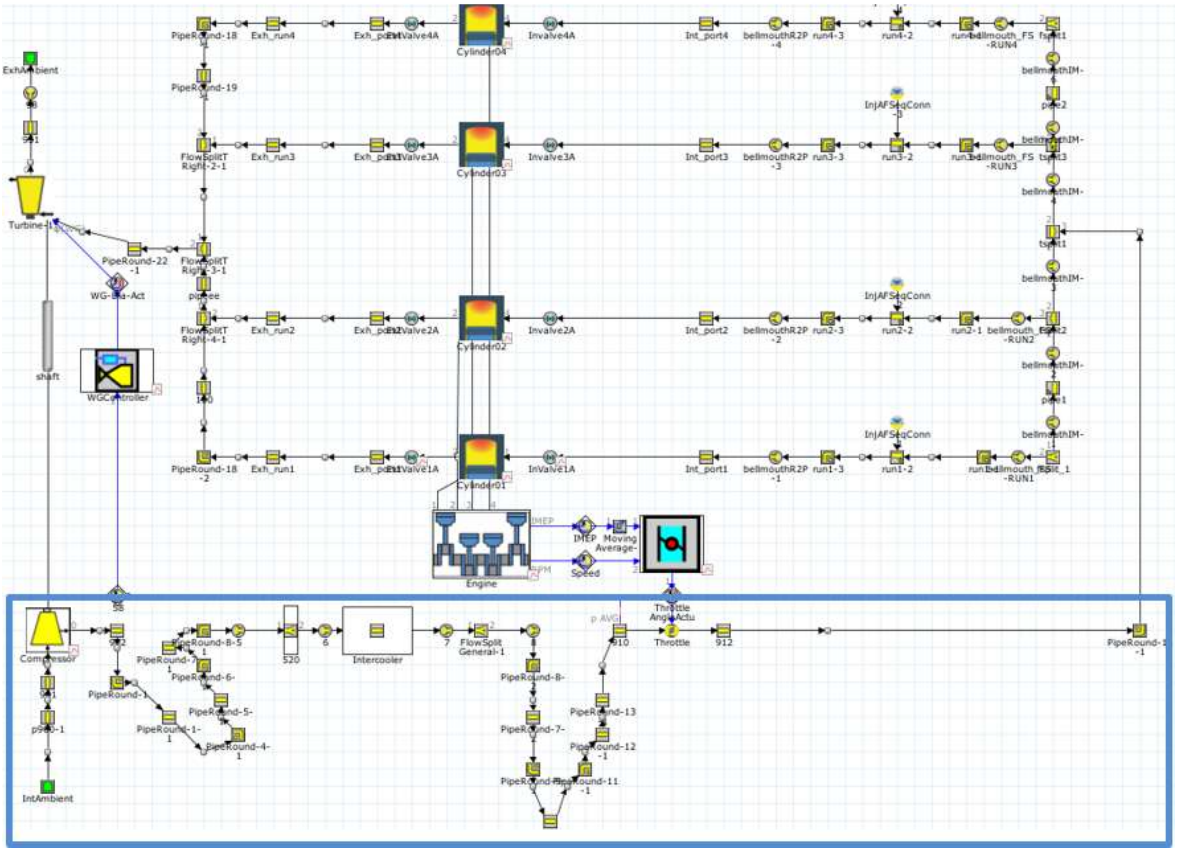

Figure 16: Blocks made through experimental measurements

The blue area (Figure 16) was built starting from the personal experimental measurements at the test bench, in the site of Westport Fuel Systems in Cherasco. The highlighted area includes all those parts of the test bench contained between the air intake and the zone downstream of the throttle valve. Each block in this area represents a portion of the pipes of the bench characterized by a specific geometry, i.e., a clearly straight or curved part, with all the related geometrical information needed by GT-Power to solve the differential equations.

A specific focus is devoted to the intercooler. Typically, this component is designed to cool the air compressed upstream by the turbocharger. Cooling the intake air not only increases its density—thus allowing a higher air mass to be inducted into the cylinder and enabling higher power output—but also reduces in-cylinder temperatures, helping to prevent knock or other abnormal combustion phenomena caused by excessive thermal levels. Typically, an air conditioning system is employed, when dealing with the test bench environment. In the present case study, the expected operating conditions foresee intake air temperatures of approximately 45 °C, as precisely requested by the constructor.

The red area (Figure 17) includes the portions of the model developed using available CAD data.

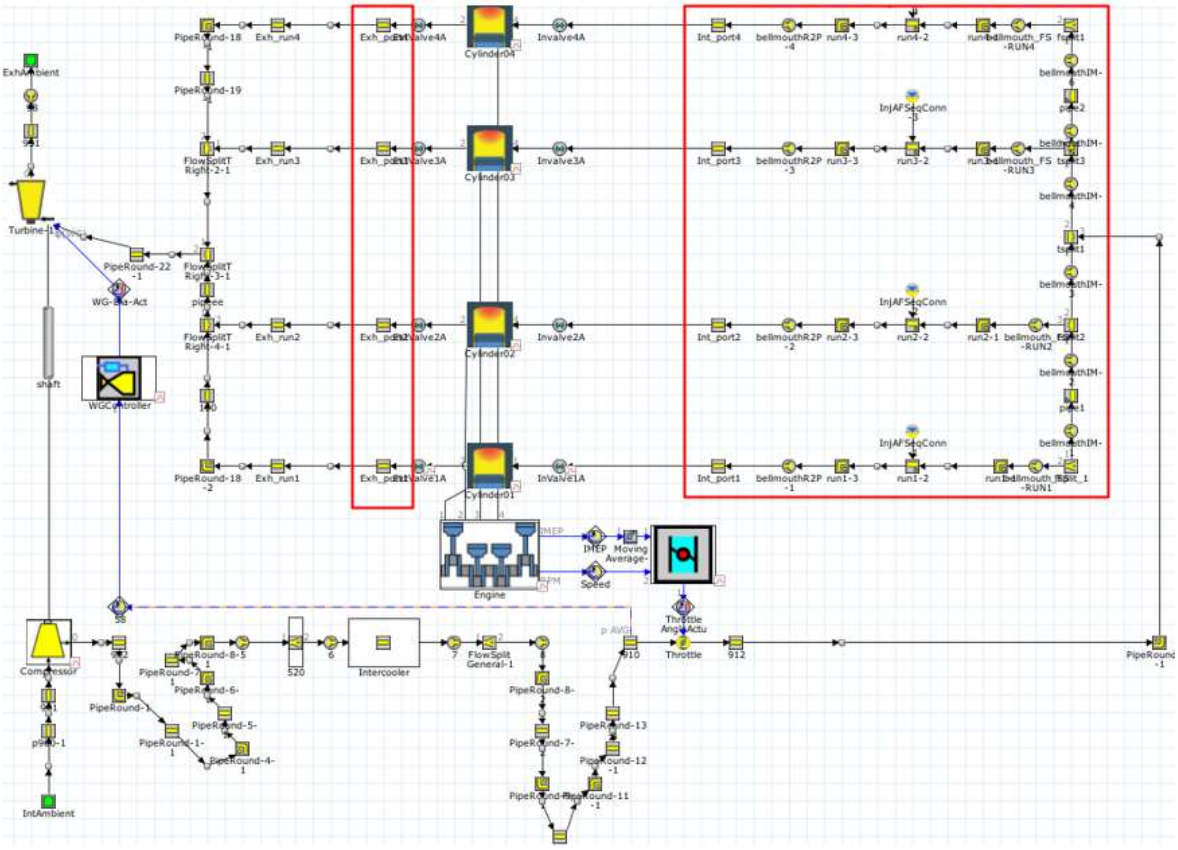

Figure 17: Areas of the model realised through the provided CAD

In particular, the CAD of the cylinder–ports assembly and the intake manifold was provided. Special attention was devoted to the intake manifold, since achieving a high level of geometrical fidelity between the real component and its numerical representation is of paramount importance for a reliable analysis. For this purpose, the GEM3D tool available in GT-Power was employed. Figure 18 offers an overview of a typical result that is accomplished through GEM3D when dealing with the CAD of the intake manifold.

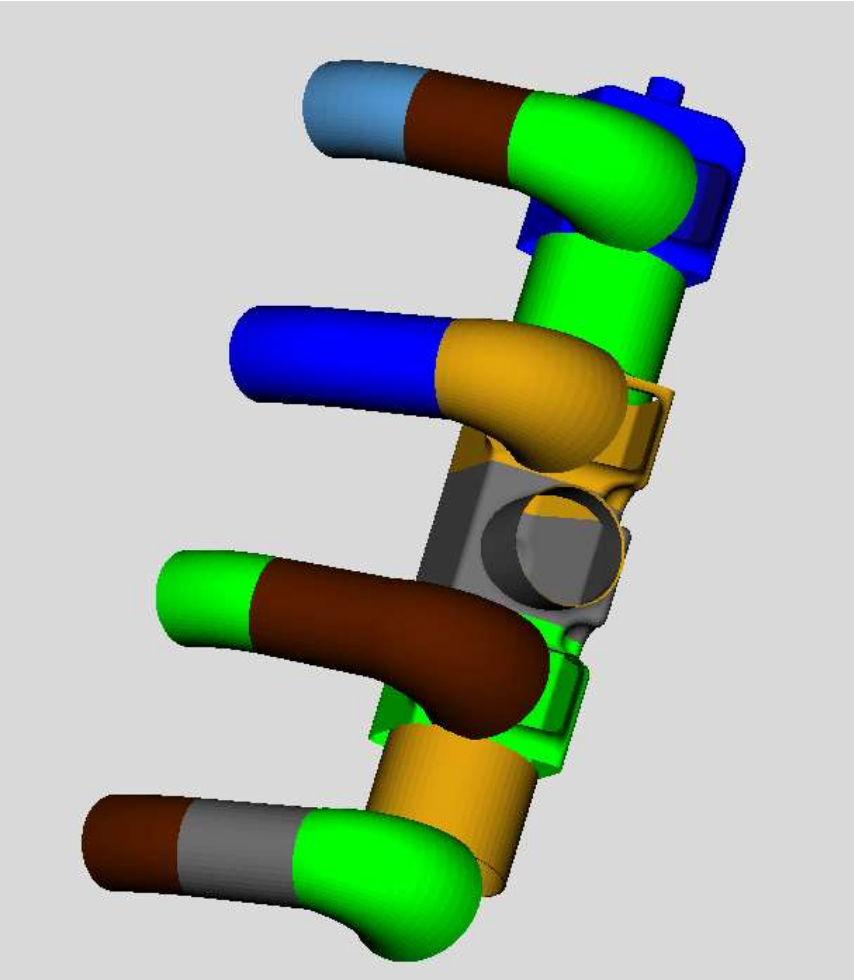

Figure 18: View of the final discretization that is assessed through GEM3D

The software allows to properly discretise the CAD in such a way to create the equivalent blocks and prevent any loss of geometrical information when passing from the CAD to the GT-Power model. Once the geometrical constraints of the part are highlighted, the flow direction is identified by GEM3D. The counterpart of the CAD in the 0D/1D model is therefore created. However, some aspects were slightly modified after the creation of the 0D/1D model, to avoid any flow loss. As clear from the zoom offered by Figure 19, each block is linked to the contiguous ones through an orifice connection.

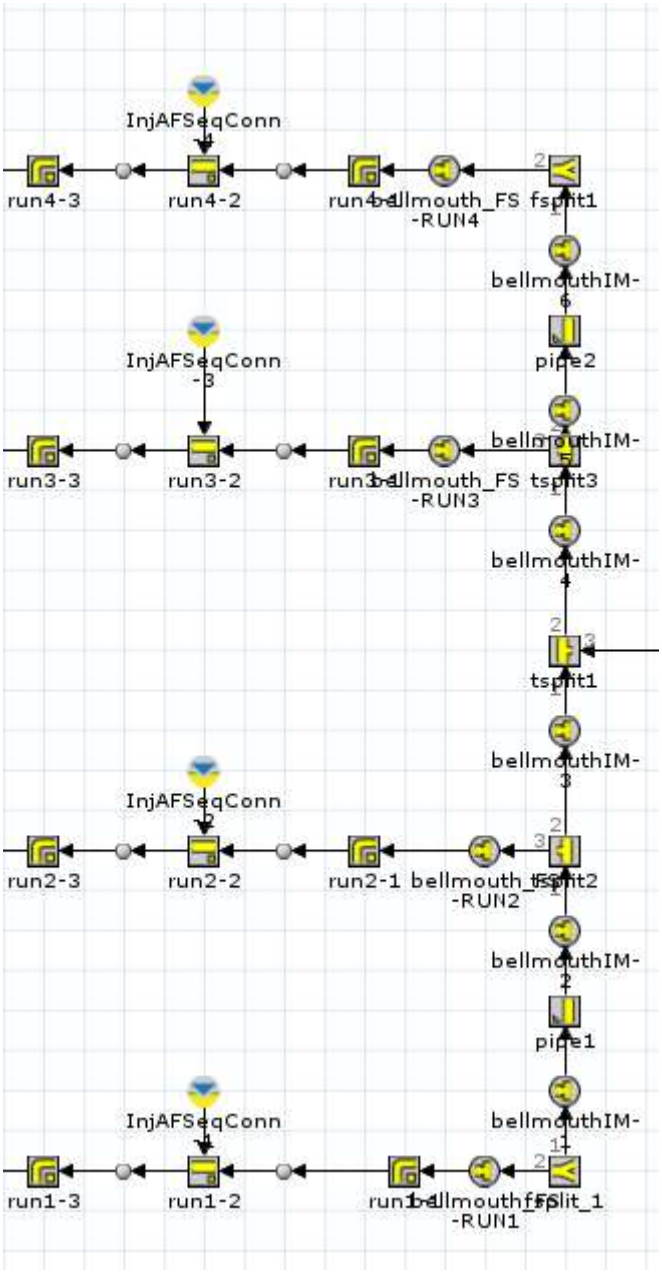

Figure 19: Counterpart of the intake manifold in GT-SUITE

In order to have continuity in terms of mass and enthalpy transport, all the orifice connections were made of the "bellmouth" typology. These kinds of orifices are characterized by unitary forward and reverse discharge coefficients (Figure 20).

Main Options

	Attribute	Unit	Object Value
◉	Hole Diameter	mm	def ...
○	Geometric Area	mm^2	
	Wetted Perimeter	mm	
	Number of Holes		def (=1) ...
	Forward Discharge Coefficient		1 ...
	Reverse Discharge Coefficient		1 ...
	Hole Thickness	mm	def (=0) ...
	Rounded Corner Radius (only if Discharge Coefficient = "def")	mm	ign ...

Figure 20: Relevant characteristics of the orifices connecting the blocks in the intake manifold

In other words, they are meant to impose that the ideal (or expected) mass flow rate and the real mass flow rate inside the pipes are equal. This is of course an ideal situation, however this is a typical and acceptable hypothesis, when dealing with 0D/1D-CFD models.

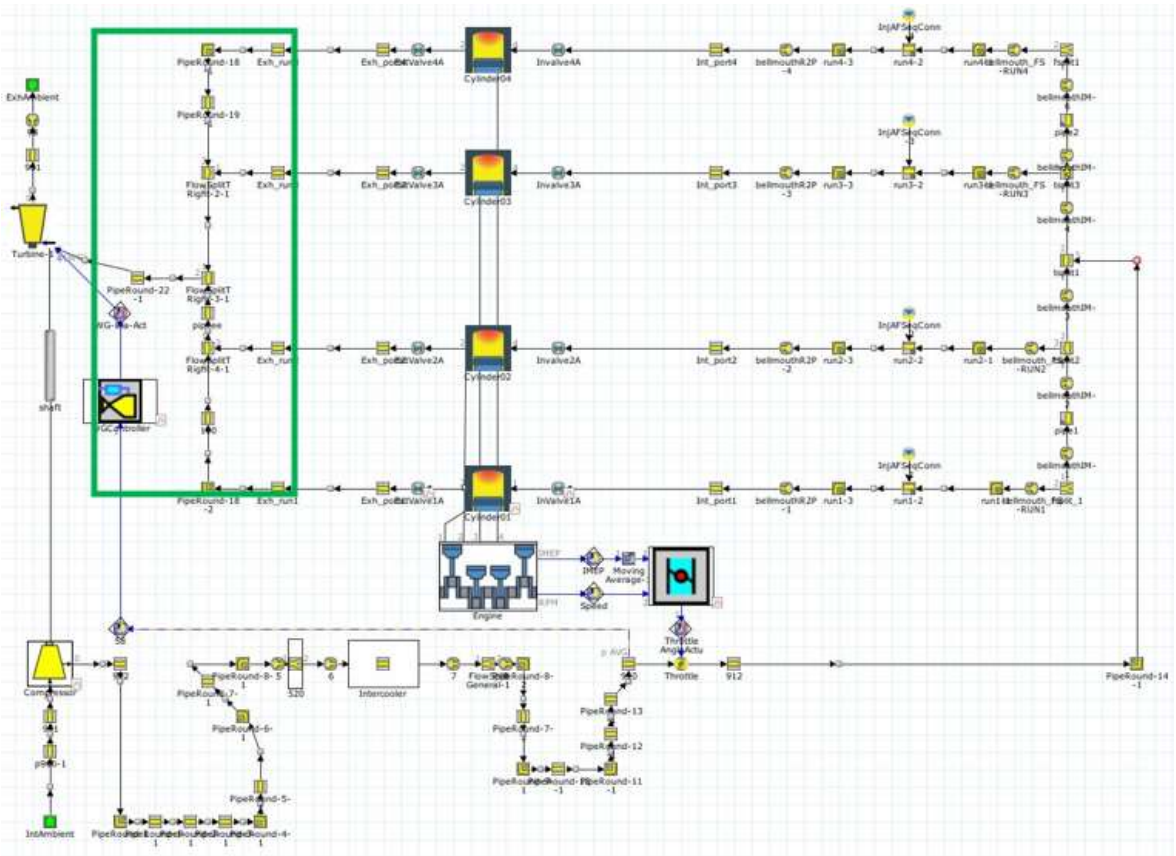

Figure 21: Area that was modelled through indirect measurements and proper hypotheses

The green area (Figure 21) identifies the blocks created based on general measurements performed on the exhaust system. Considerable effort was dedicated to this part of the model, as the exhaust pipes are subject to the most intense thermal exchange. Several parameters required for an accurate correlation between model and experimental data could neither be measured nor retrieved. Among these, the exhaust pipe wall thickness represented a critical unknown. This issue was addressed through a simple Design of Experiments (DoE) approach, involving a sweep of both wall thickness and heat transfer multiplier values, allowing to find. The optimal configuration was identified as the wall thickness–heat transfer multiplier pair that ensured the exhaust temperature trace at the turbine inlet remained within a reasonable error band across the considered operating conditions (in the order of 70 K, as better explained further on in this chapter).

Once the geometrical model was completed, the control strategy and the general model characteristics were implemented.

4.2 Fundamental characteristics of the model

One of the most important characteristics of the model that allows to fully understand the logic beyond this analysis is that this case study refers to an air-to-fuel ratio-imposed and combustion-imposed model. The air-to-fuel ratio is imposed through the blocks of the injectors, and the combustion is imposed by overriding the experimental burn rates to those set by default through the Woschni's model (Figure 22 and Figure 23).

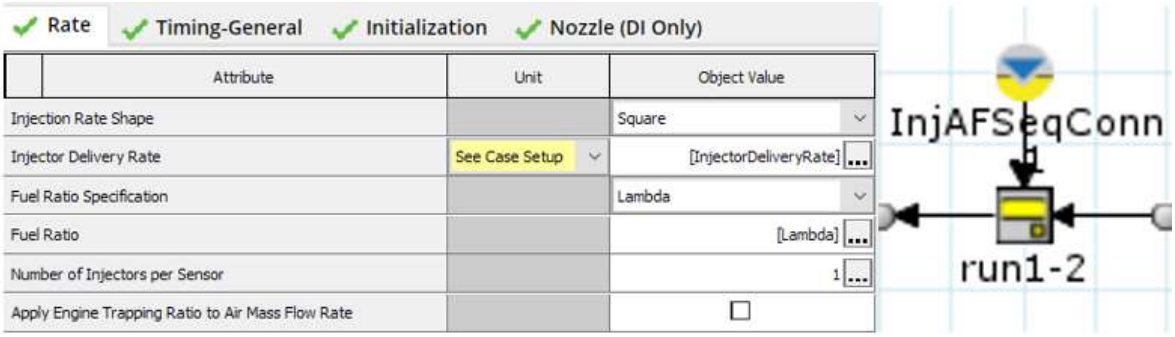

Figure 22: Relevant specifics of the injectors

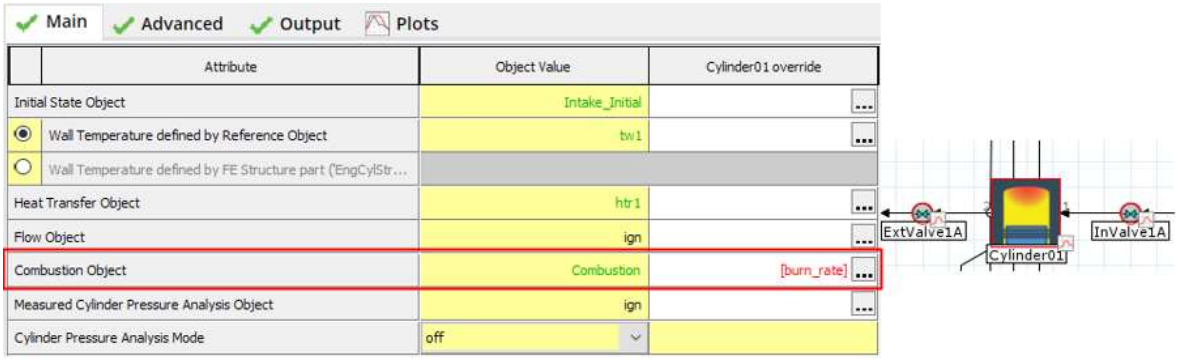

Figure 23: Main setup of the cylinder in the imposed-combustion model

In other words, thanks to the provided pressure cycles recorded at the test bench of Westport Fuel Systems, it was possible to retrieve the corresponding burn rate inside the cylinder. This passage is realised through a so-called Cylinder Pressure Oscillation Analysis (CPOA) (Figure 24).

In the context of the imposed-combustion model, this single-cylinder analysis requires few, specific inputs:

- The recorded cylinder pressure trace, against the crank angle
- The spark timing
- The end point of the analysis – in this case, the Exhaust Valve Opening (EVO).
- The number of temperature zones – in this case, the two-temperature zones was employed, to account independently for the burned gas and the unburned gas.

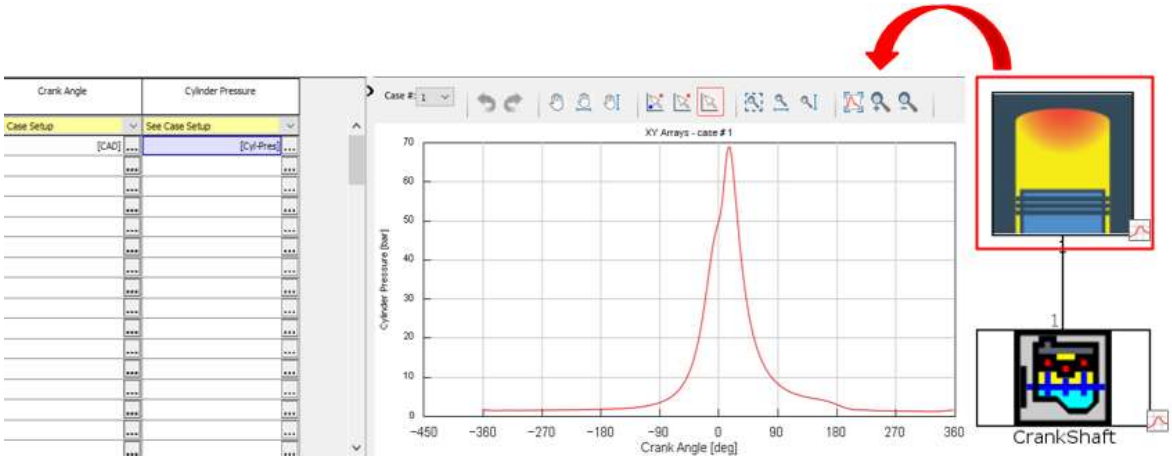

Figure 24: Build-up of the CPOA and setup of the experimental pressure cycles

The CPOA provides two outputs:

- A file containing the burn rates associated to each simulated case, that can be subsequently transferred into the complete model
- A file containing a graphical report of the trend of simulated quantities against the experimental ones against the sweep of any variable present in the model, typically the crank angle.

The report file must be checked for what the relevant quantities are concerned, in our case the log(p)-log(V) diagram and the LHV multiplier graph. The log(p)-log(V) trace of the simulation should be as close as possible to the experimental one (Figure 25).

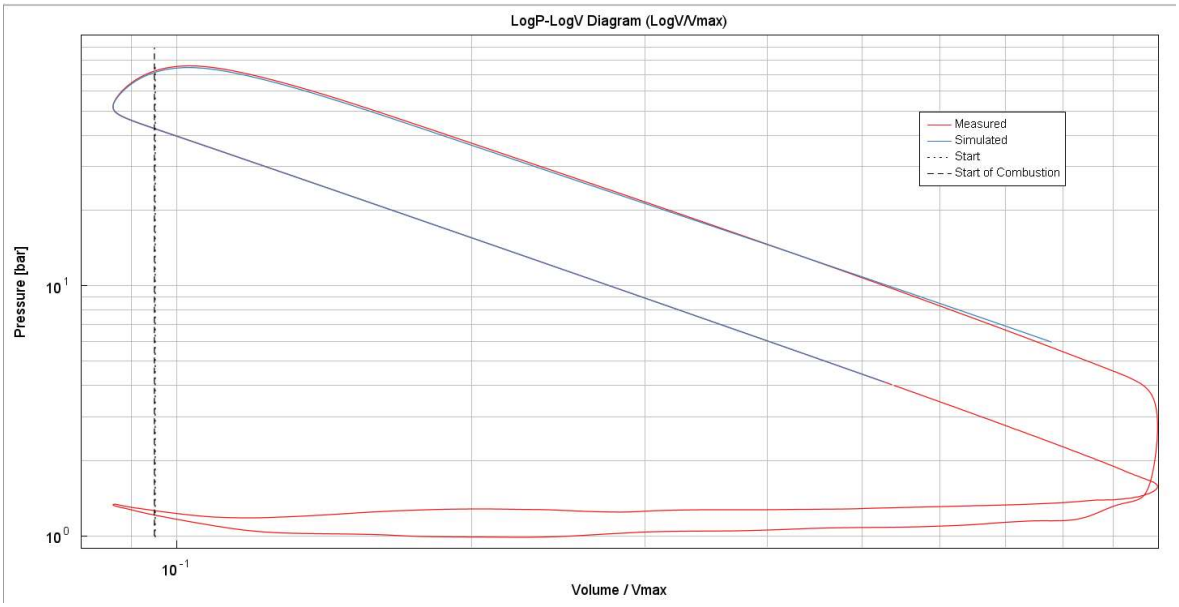

Figure 25: log(p)-log(V) diagram of a typical engine cycle of a well calibrated CPOA

In case of clear mismatch, adjustments can be made on the settings of the model to try and match the experimental results, basing on where the mismatch occurs. The other curve to be checked is then that related to the LHV multiplier, relative to each case. Each point must be as close as possible to 1, with a maximum tolerance of 10% (Figure 26). This because the LHV multiplier leads the output burn rate, in particular:

- LHV multiplier < 1: the model overestimates the heat release, therefore the multiplier must compensate the heat excess
- LHV multiplier > 1: The model underestimates the heat release, so the multiplier aims at adding what is missing.

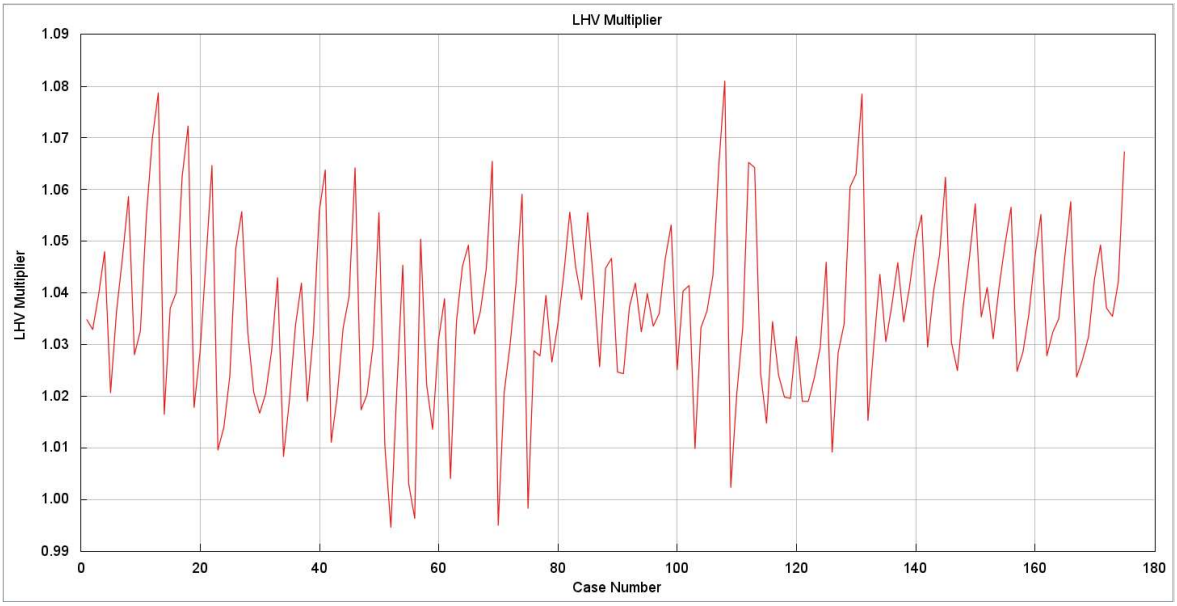

Figure 26: Obtained LHV multiplier graph of the CPOA

Of course, a perfect match is not expected at all, yet the aim is to minimise the mismatch with respect to these quantities, in order to obtain representative burn rate to impose in the model. From last figure, it is possible to see that the model tends to slightly overestimate the heat release. This can be ascribable to an overestimation of the combustion efficiency, however, the mismatch is contained within the error margin that was previously established.

A brief focus on the CPOA is worth of space in this thesis, as this procedure effectively allows the extraction of additional experimental information. In particular, as anticipated, the focus of the presented analyses is on indicated quantities, which are more representative of the combustion process itself and help compensate for missing data. For example, while Westport Fuel Systems provided Brake Mean Effective Pressure (BMEP) values, Indicated Mean Effective Pressure (IMEP) measurements were not available, due to the complexity and cost of the measurement process. However, IMEP was retrieved through the CPOA, allowing the computation of the Friction Mean Effective Pressure (FMEP):

$$FMEP = IMEP - BMEP$$

The availability of experimental FMEP is particularly valuable, as it enables, for instance, the direct imposition of friction losses within the crank train model without relying on empirical friction models such as the Chen–Flynn formulation, which would require additional calibration and typically introduces compromises in accuracy. Regarding the control strategy, two controllers were employed, as shown in Figure 27 and Figure 28. The wastegate (WG) valve controller targets the experimental boost pressure and receives as input the pressure upstream the throttle valve, as highlighted in Figure 27. The controller actuates on the valve opening basing on the thermodynamic conditions at the turbine inlet,

i.e., the available enthalpy. Opening the valve diverts energy away from the turbine, which is typical of operating points requiring low boost pressure, while closing the valve increases turbine power to achieve higher boost levels, typical of high/full load operations.

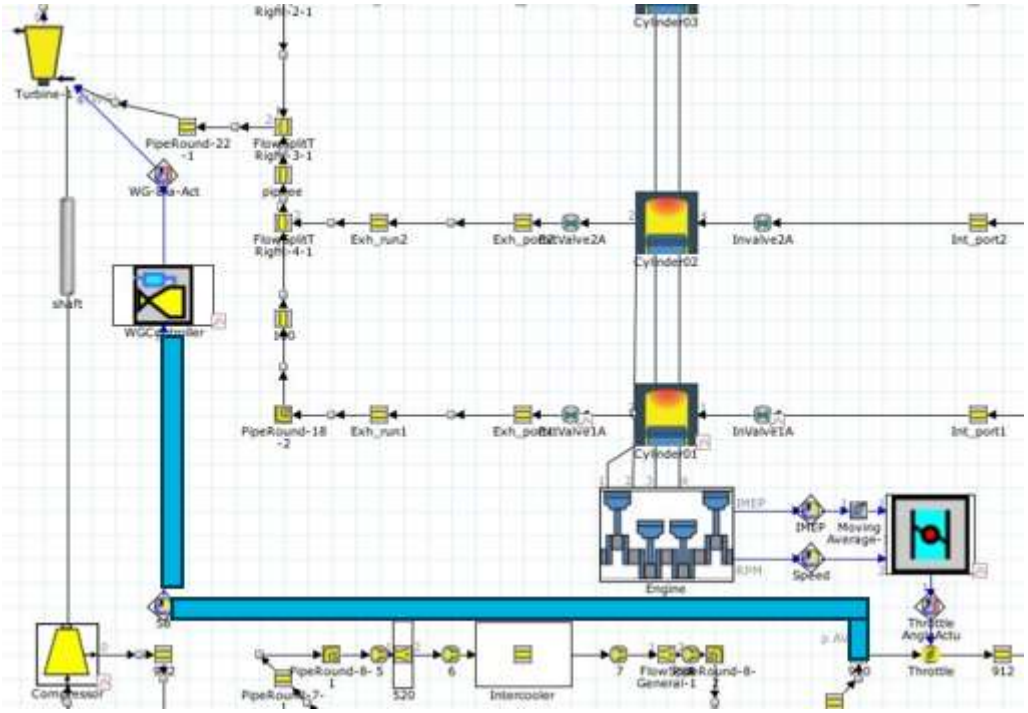

Figure 27: Input of the controller of the Wastegate valve

The controller on the throttle targets the experimental IMEP (retrieved from the CPOA) and commands the minimum opening of the throttle that is necessary to entrain the amount of air that – given the lambda that is imposed inside the injectors – allows to reach the MEP inside the cylinder (Figure 28).

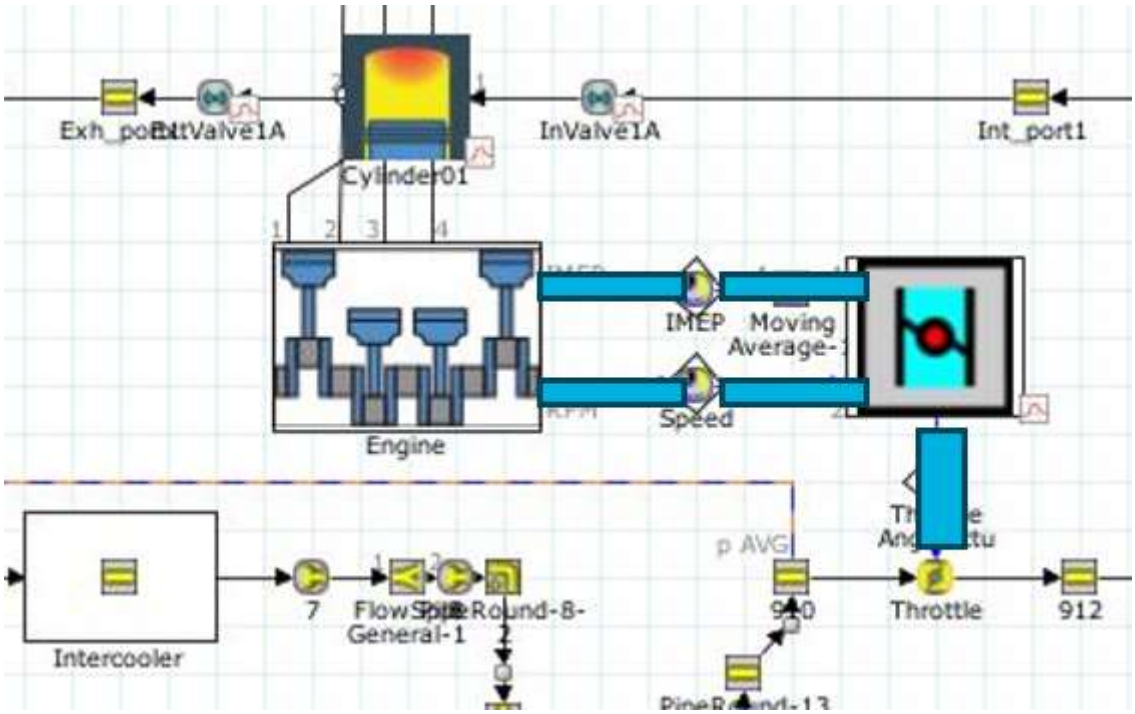

Figure 28: Input and actuation of the controller of the throttle valve

The two controllers are not independent one from each other. A typical critical scenario (that occurred during the analyses as well), is the non-convergence of the controller of the Wastegate valve, thus the impossibility of reaching the boost level, therefore the experimental IMEP cannot typically be matched, since the necessary air flowrate was not reachable, thus leading to the non-convergence of the controller of the throttle valve as well. However, the convergence of a controller does not necessarily imply the convergence of the other.

4.3 Correlation plots

A discussion on the correlation diagrams deserves to be done with the due critic sense. For this correlation, the typical tolerance of ±5% was applied. In cases like the temperature in the main blocks of the exhaust system, in fact the absolute error was considered, in light of the hypotheses and the approximations that had to be done. In a correlation diagram, the reference is with respect to a certain quantity (e.g., the air flow rate) and the coordinates of a point are the experimental value and the simulated one. Preliminarily, the diagrams regarding the controlled parameters can be presented. Clearly, since the controllers always reached the convergence, the trace follows the bisector of the diagram.

This is the case of the boost pressure, the IMEP720 (i.e., gross of the pumping work) and the FMEP (Figure 29 and Figure 30).

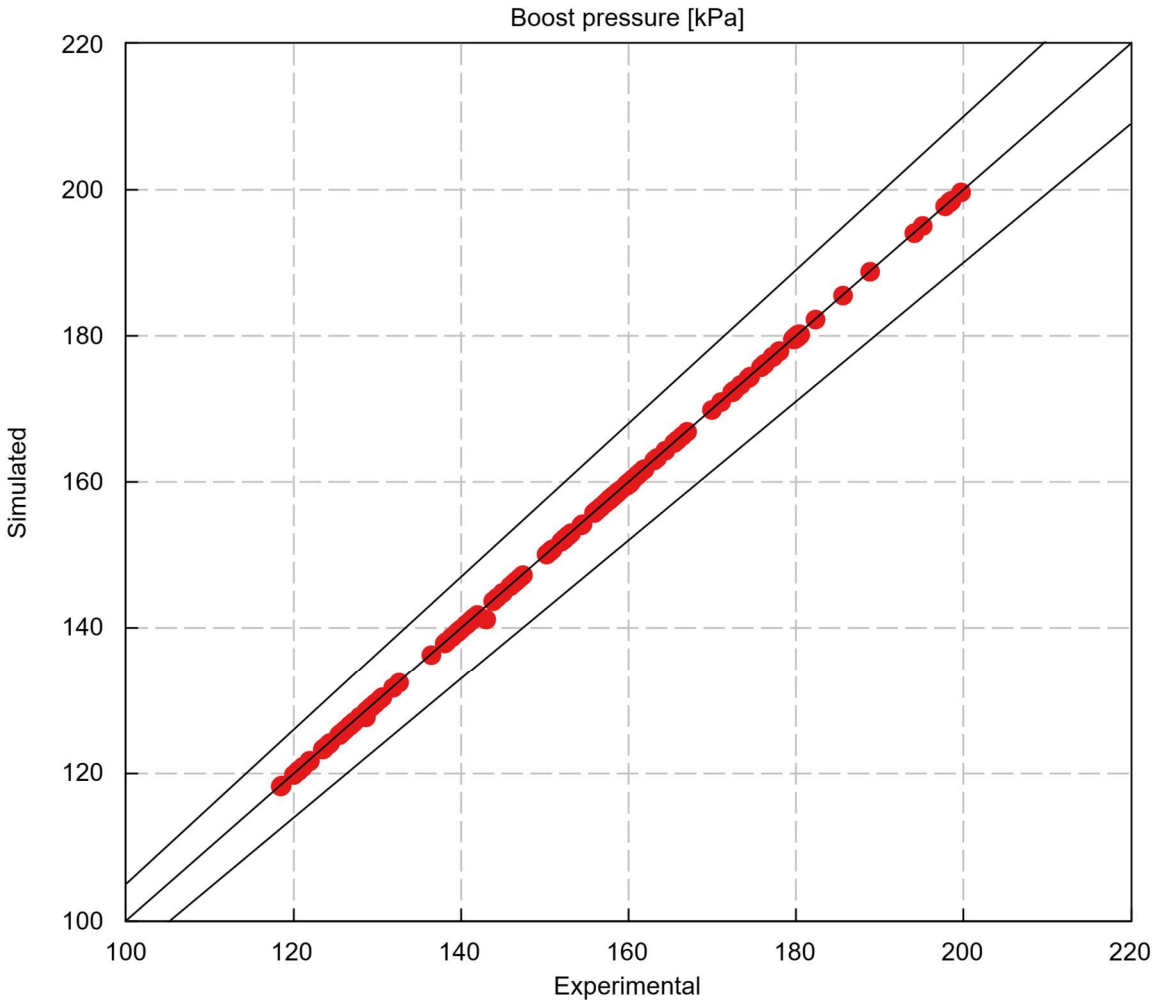

Figure 29: Correlation plot of the boost pressure

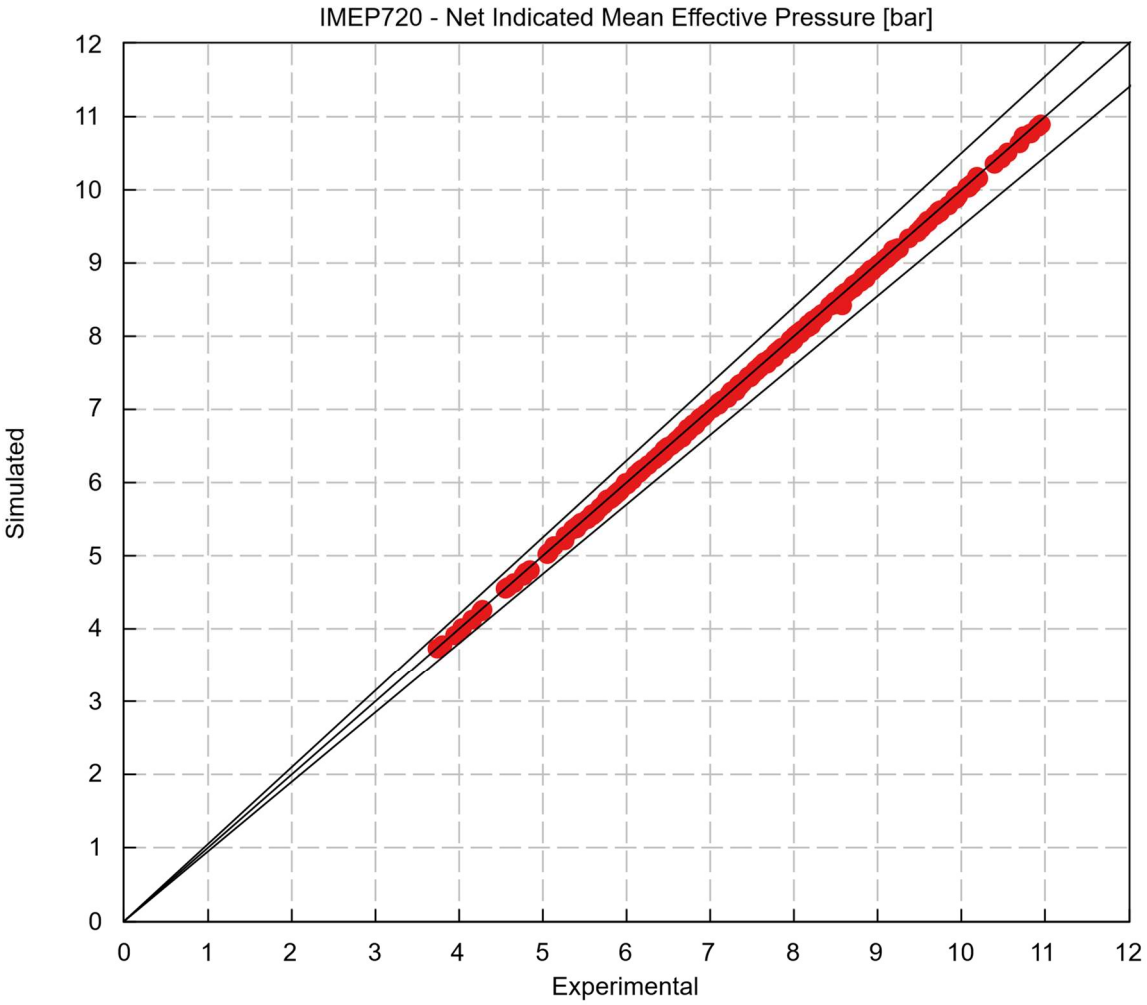

Figure 30: Correlation plot of the IMEP

Before entering the details of the performance parameters, an aspect of paramount importance should be highlighted, in order to read the results with the proper hypotheses made well clear.

Figure 31 shows the correlation diagram of the average pressure inside the intake manifold.

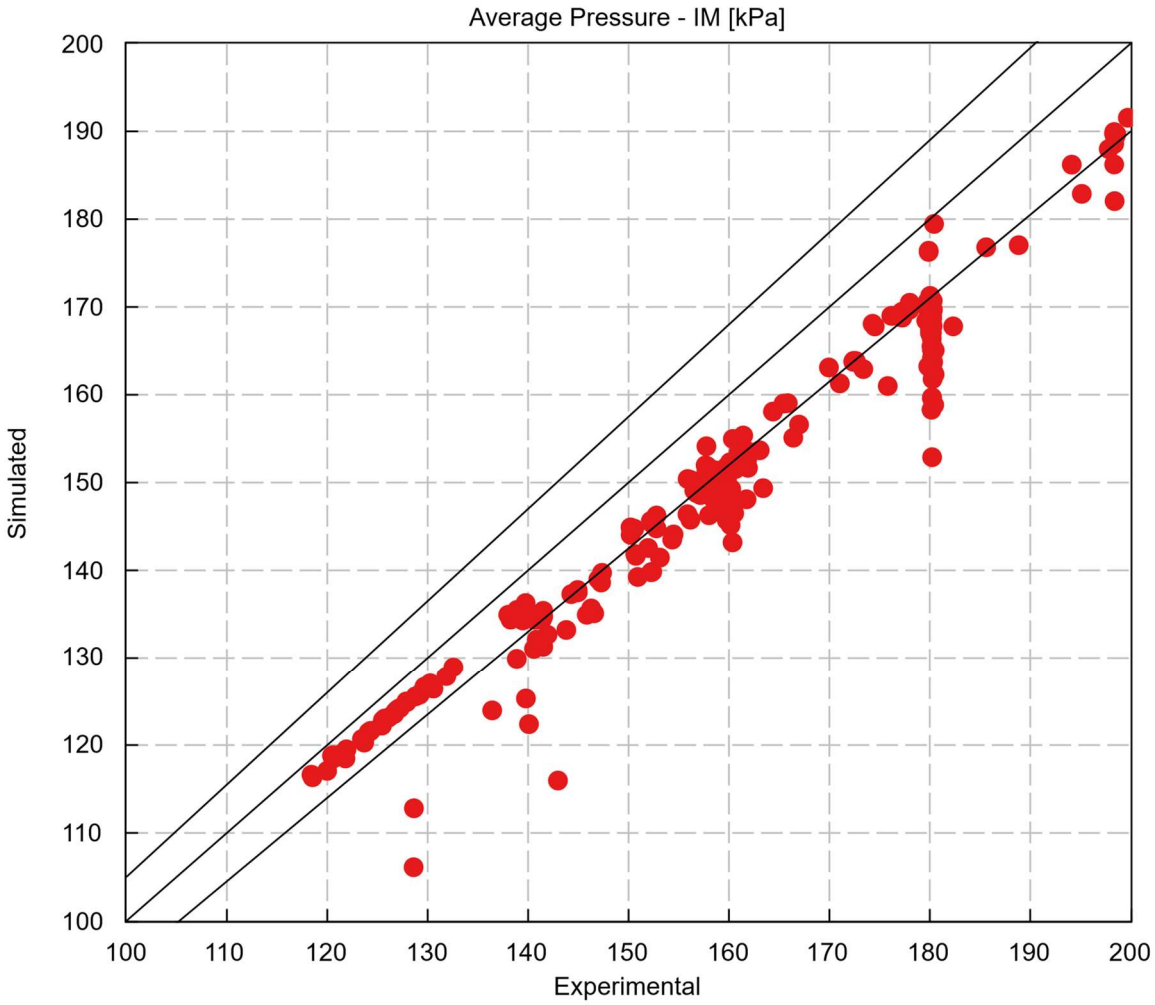

Figure 31: Correlation plot of the average pressure in the intake manifold

As visible, the correlation is overall solid, however a slight underestimation of the model with respect to the experimental data is present. This discrepancy can be explained considering two points of view.

First, when dealing with experimental data, a check of the provided dataset is necessary. Those points that result well out of the ±5% tolerance are characterised either by a remarkable gap between the boost pressure and the intake manifold pressure, at the test bench; therefore, this point might have been influenced by some issue that occurred during the measurements at the test bench and that could not be modelled inside the GT-SUITE environment due to the lack of information in this sense(Figure 32).

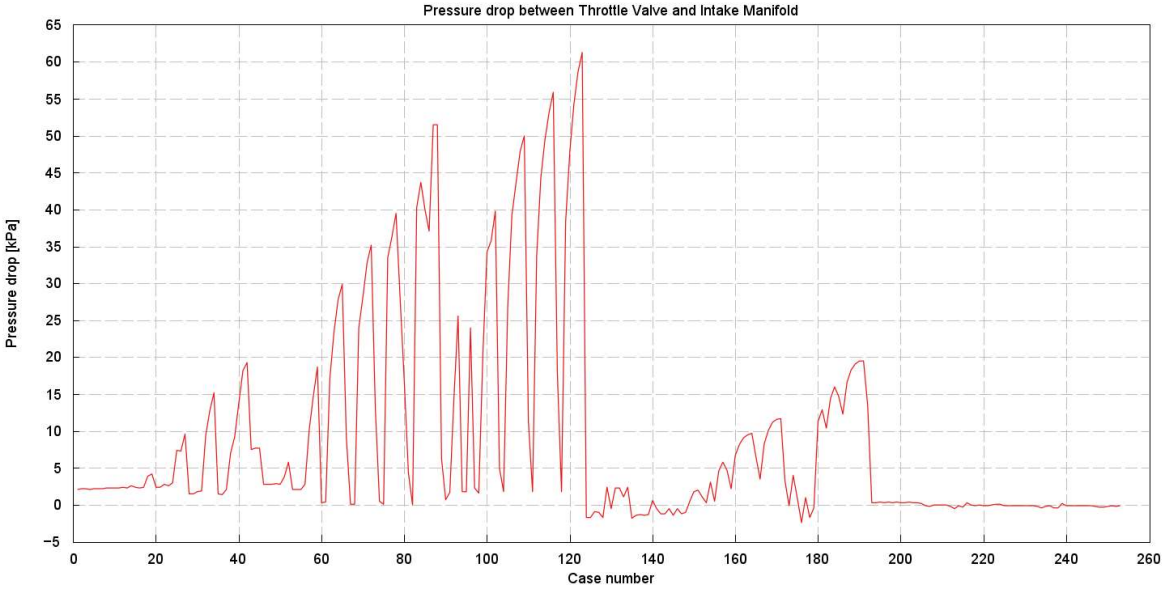

Figure 32: graph of the pressure drop between the throttle valve and the intake manifold

Nevertheless, not all the points that are not within the tolerance show either this aspect, or other clear criticalities. Therefore, the focus can be moved towards the results of the CPOA: as anticipated above in this chapter, by looking at the LHV multiplier graph once again, the results are globally acceptable, however, a likely occurrence is the overestimation of the combustion efficiency in the model (Figure 33).

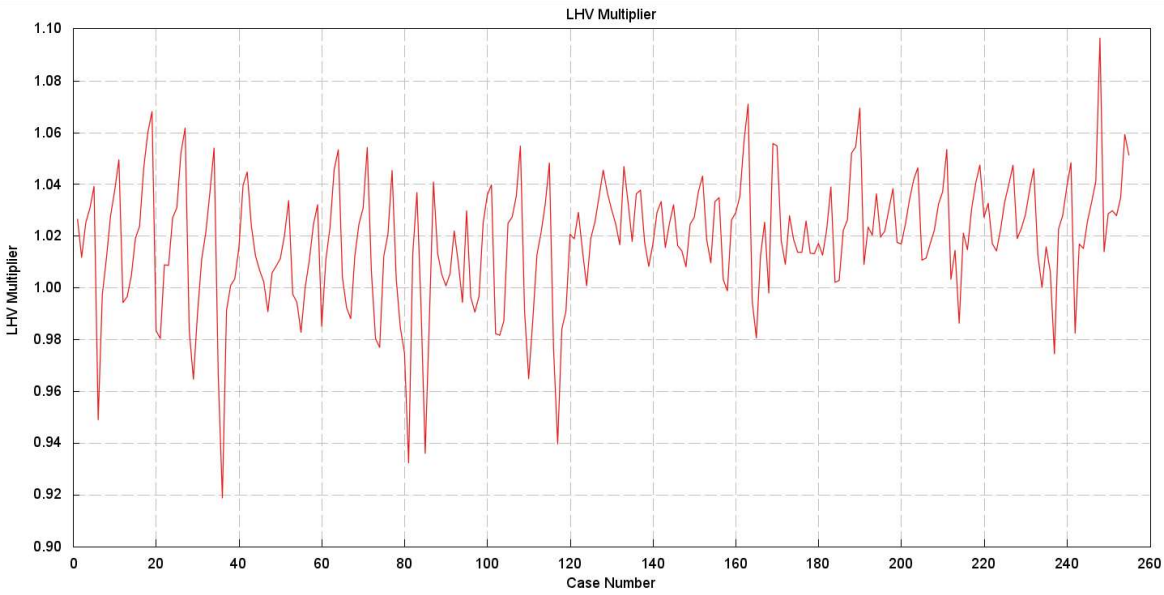

Figure 33: graph of the LHV multiplier obtained from the CPOA

This is well supported by the fact that the experimental tests were conducted at Wide Open Throttle (WOT), while by looking at Figure 34, the maximum throttle angle in the model is in the order of 45° and it reaches 90° just in once.

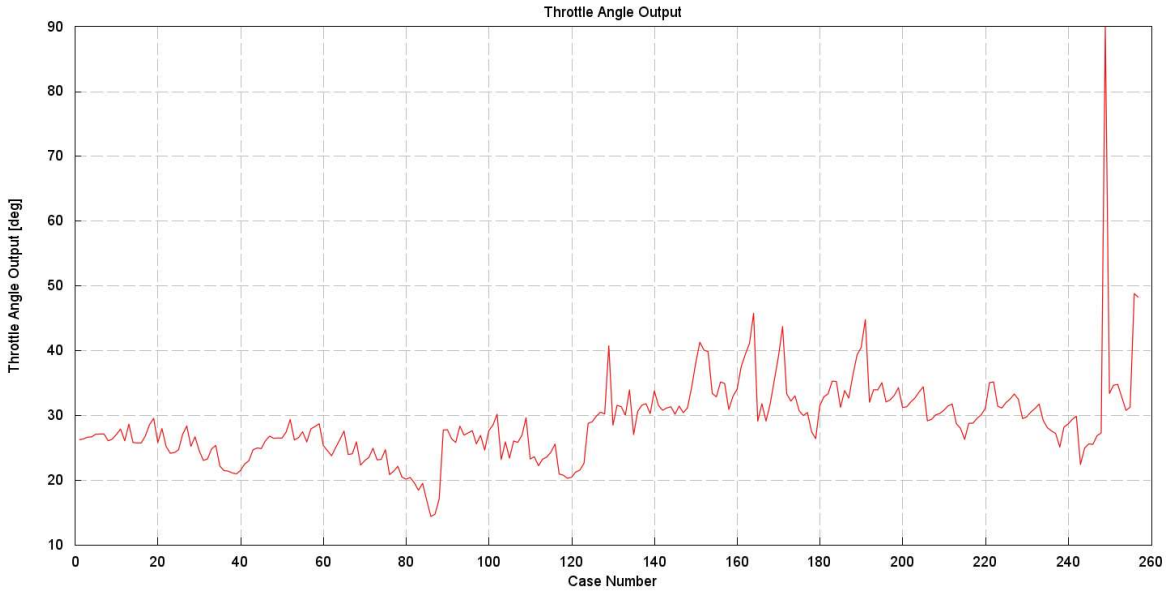

Figure 34: trace of the output throttle angle for each analysed case

However, this is balanced by the fact that the air-to-fuel ratio is imposed. This means that despite the gap in terms of throttle angle, a strong correlation in terms of air flow rate and fuel flow rate is guaranteed, as clear in Figure 35 and Figure 36.

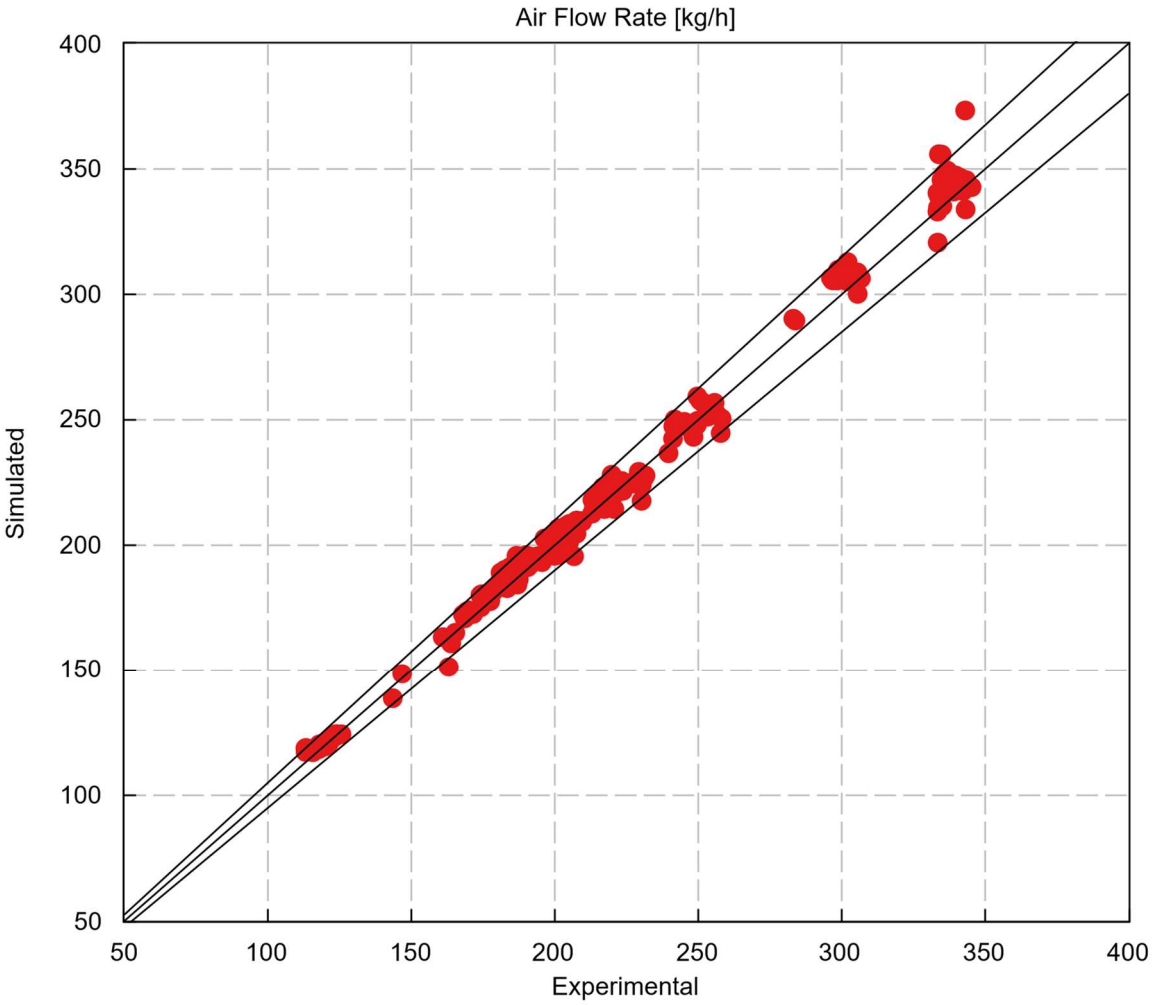

Figure 35: Correlation plot of the air flow rate

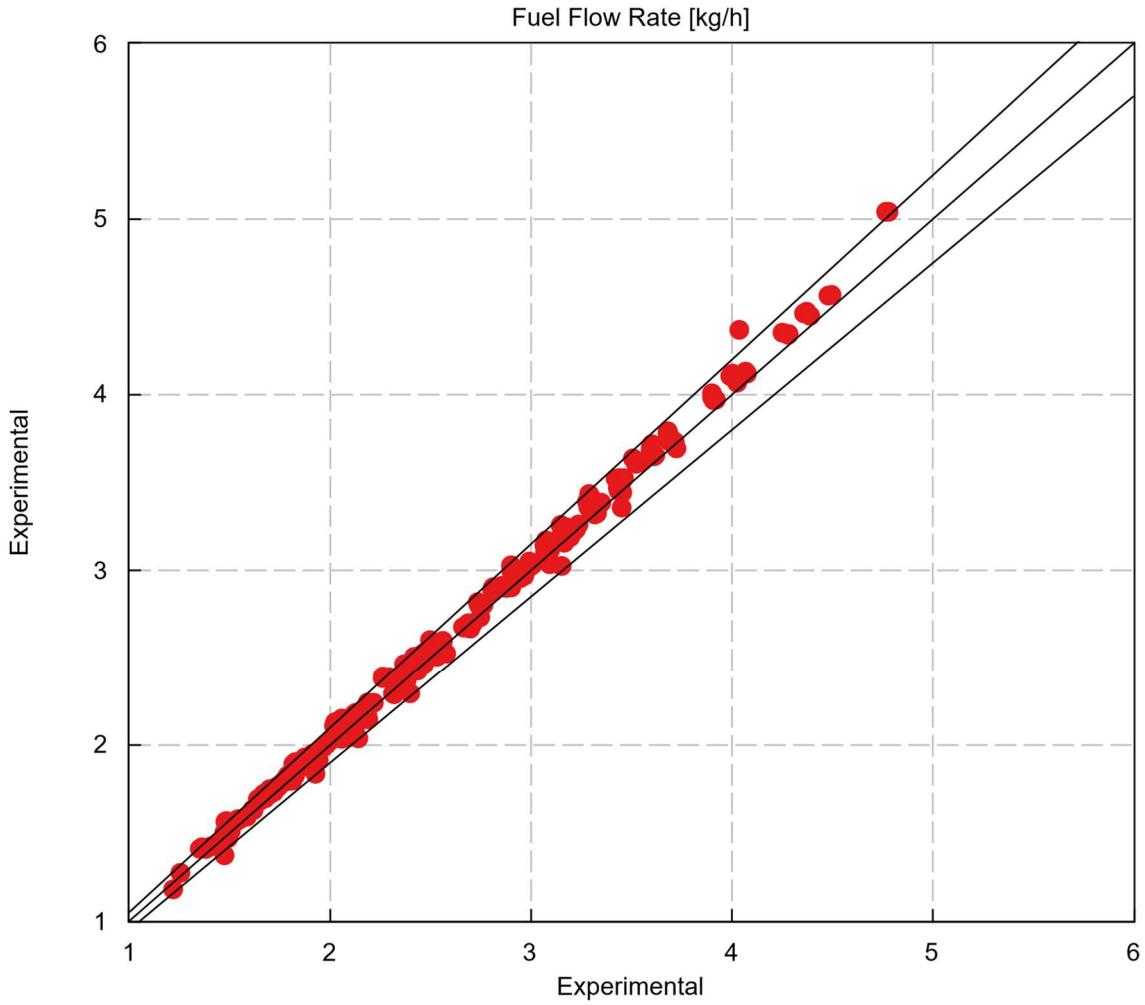

Figure 36: Correlation plot of the fuel flow rate

The reliability of the presented model is furthermore supported by the strong correlation that was obtained throughout the exhaust line. This because, as previously shown in the introduction, the quantity of provided information did not allow for a punctual modelling of this area of the model, thus leading to the need of relying on some geometrical and thermodynamical approximation (e.g., finding a proper wall thickness and calibrating the heat transfer multiplier). Figure 37 shows the pressure at the turbine inlet.

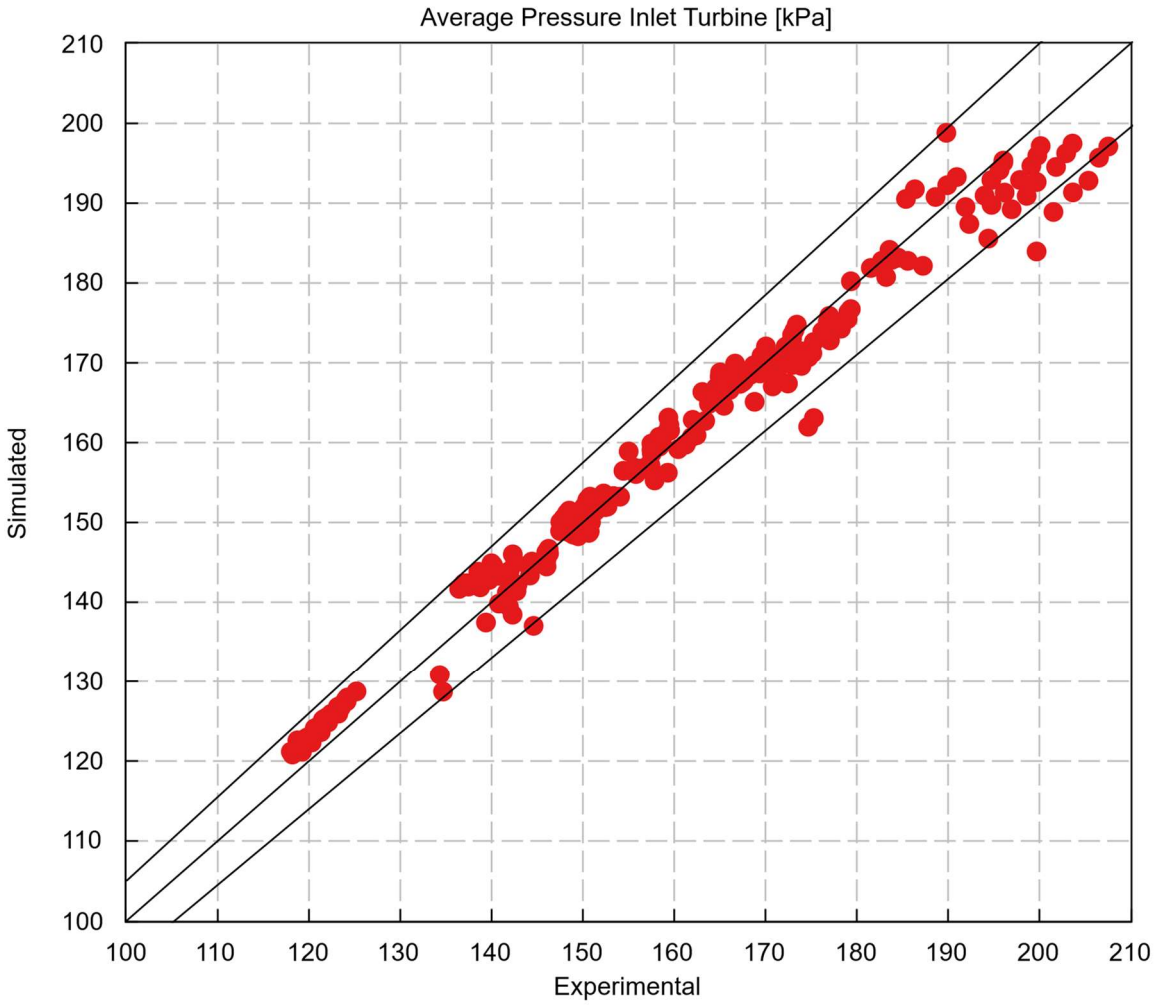

Figure 37: Correlation plot of the pressure at the inlet of the turbine

The correlation of this quantity has a strong influence on that of the Brake Specific Fuel Consumption (bsfc) – of course, together with the correlation of the air flow rate and that of the IMEP – that is shown in Figure 38. This happens because the inlet turbine pressure directly influences the pumping loop and so the net-work extraction from each cycle. In this case study, that considers a turbocharged engine, this aspect is further enhanced, since the pumping loop is capable of providing a positive contribution to the extracted work.

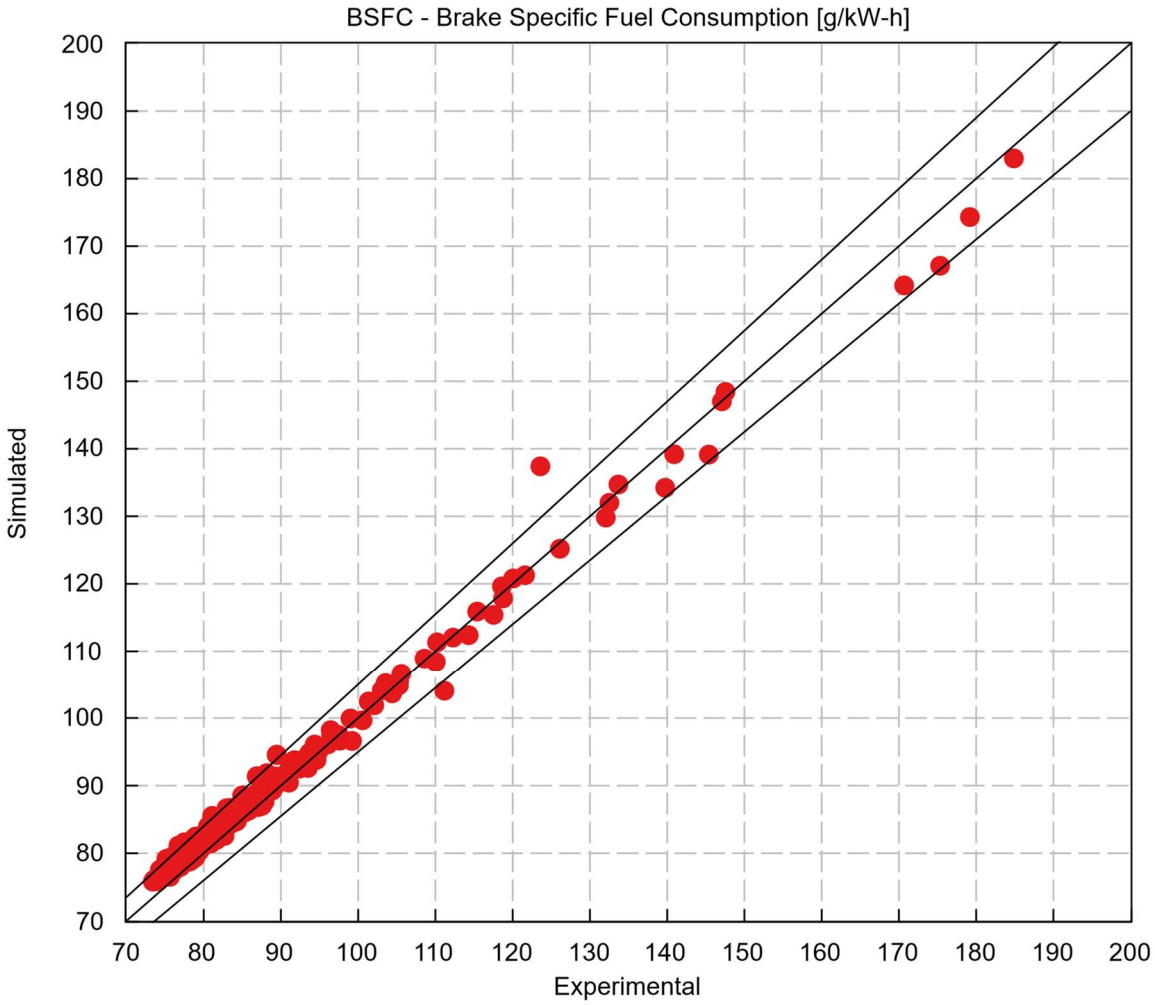

Figure 38: Correlation plot of the Brake Specific Fuel Consumption

Regarding the temperatures, Figure 39 and Figure 40 show the temperatures at the level of the exhaust runner and that at the level of the inlet of the turbine.

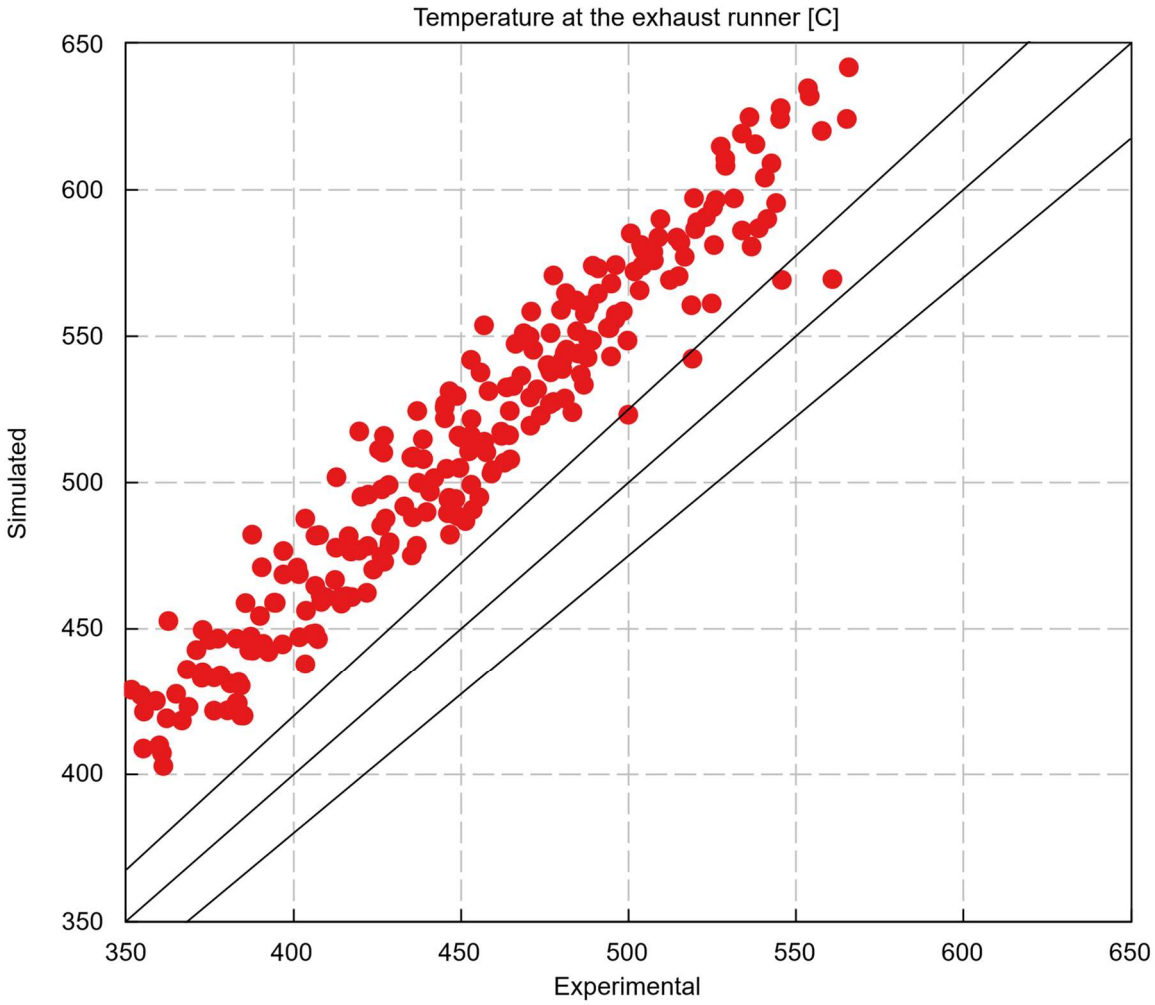

Figure 39: Correlation plot of the temperature at the exhaust runner

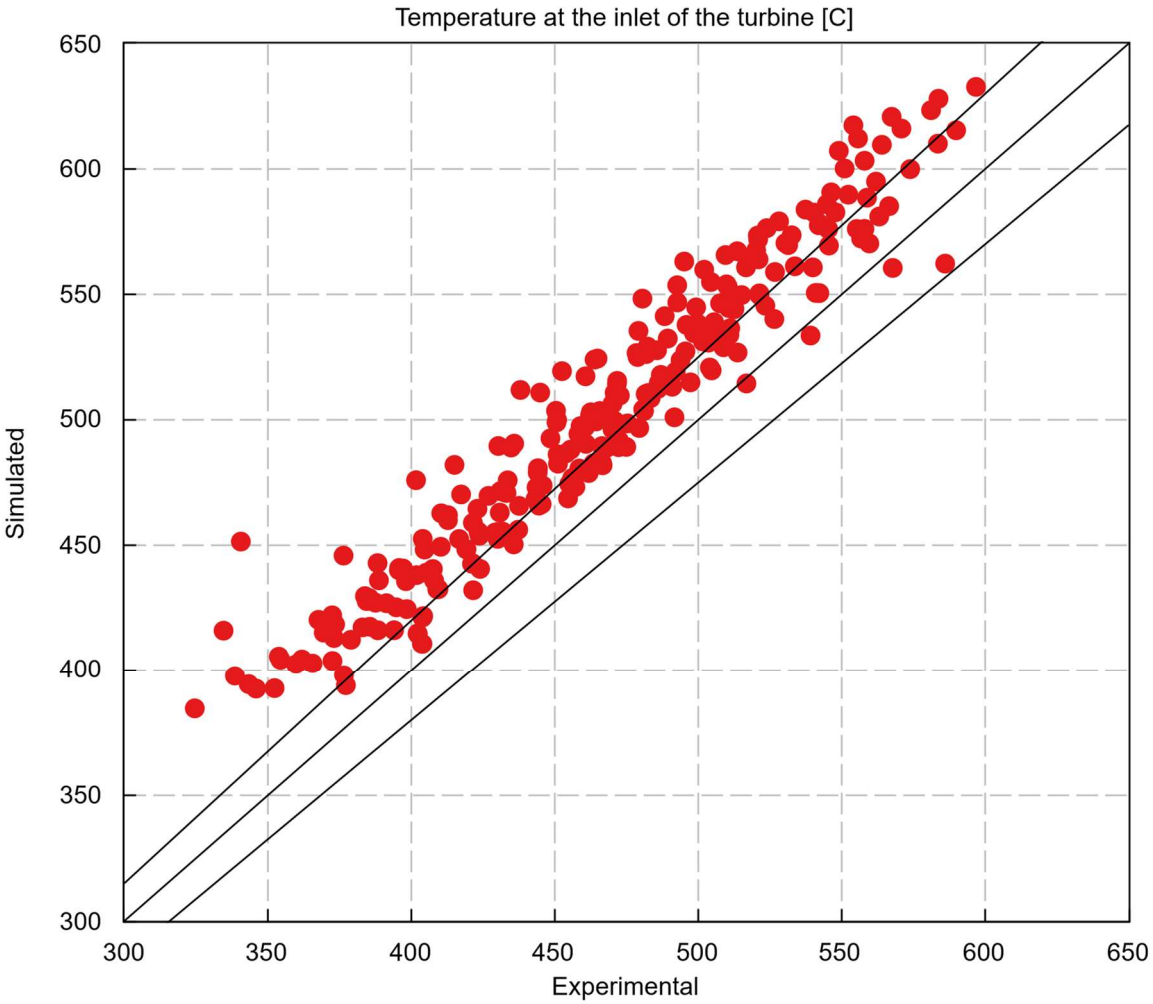

Figure 40: Correlation plot of the temperature at the inlet of the turbine

Despite on average both the plots present an overestimation of the model with respect to the experimental data that is out of the tolerance in terms of percentage, the absolute error is way acceptable, especially in light of what was done in terms of modelling of the blocks of the exhaust line.

As a conclusion for this chapter, it is clear how a model that is overall well representative of the engine installed at the test bench is available at the level of this analysis, thus allowing for the accomplishment of the subsequent steps of this project, i.e., the development of the predictive model.

5. Development of the H2 predictive combustion model

5.1 Methodology

The development of the predictive combustion model foresees two main phases, each characterised by a type of single-cylinder analysis. First, a Three Pressure Analysis (TPA) is foreseen. The intended three pressures are the intake pressure, the exhaust pressure and the in-cylinder pressure. The TPA in this case study is exploited for its capability of performing the prediction in terms of turbulence of the flow entering the cylinder, therefore its calibration is crucial for having a good final prediction of the combustion process, since the primary role in the phenomenon of combustion covered by turbulence. In this analysis, two look-up tables coming from the results obtained by the 3D analysis – that was conducted in parallel to this thesis – were used as reference for the output quantities of interest, i.e., the Turbulent Kinetic Energy (TKE) and the Turbulent Length Scale (TLS). Various optimizations were made through the GT-SUITE optimizer, to find the optimum combination of the multipliers that govern the equations of the TKE and TLS along the engine cycle. Subsequently to the calibration of the TPA, the CPOA can be performed. A multi-factorial optimization will be carried on in an analogous fashion as made with the TPA, thus finding an overall value that unites the combustion phenomenon in terms of dilution, flame kernel growth, turbulent flame speed and Taylor length scale, that will then be validated against the experimental dataset, so to have the final material to accomplish the final step, i.e., the implementation inside the complete model.

5.2 The Three Pressure Analysis (TPA)

The TPA is the first step for the construction of the predictive model. This type of analysis is generally employed for obtaining a burn rate from the experimental data, nevertheless in this case study the objective is to calibrate a predictive model, that can be eventually built through a CPOA. However, the TPA can be exploited for calibrating the parameters that govern the turbulence the flow enters the cylinder. For the scope of predicting the burn rate, the correct forecast of the turbulence – in particular, of the Turbulent Kinetic Energy (TKE) and of the Turbulent Length Scale (TLS) – is crucial. Since this case study deals with a PFI engine, the development of a flame front in the combustion chamber is foreseen. Turbulence modifies the shape of the flame front by wrinkling it, thus increasing the available contact surface and so the speed of its development. In this thesis, a steady TPA will be assessed, therefore the input pressure cycle will be the ensemble average of the pressure cycles measured at the test bench. Figure 41 shows the blocks representative of this analysis.

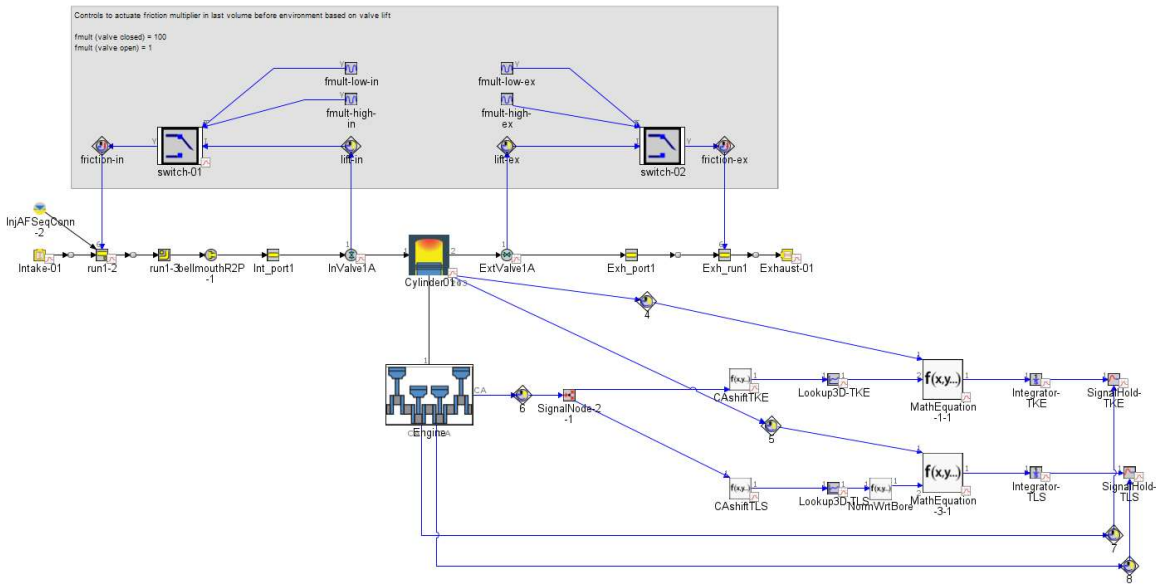

Figure 41: General overview of the Three Pressure Analysis made for the turbulence parameter optimization

The setup includes:

- Intake port pressure and temperature
- Exhaust port pressure
- Cylinder pressure
- Fuel injection data
- Spark timing

What is accomplished in practice in this case is to consider the portion of the model contained within the block associated to the part of the runner the injector is connected to (in Figure 41, the block *run1-2*) and the block of the exhaust runner. The extremes of the model are two blocks *BoundaryPressureTPA*, specifically included in the library of GT-SUITE for this analysis and better shown in Figure 42.

Attribute	Unit	Object Value
Instantaneous Pressure	bar	P-intake-inst
Crank Angle Array for Multi Cycle Data	deg	ign
Time-Averaged Pressure/Pressure Shift (Multi Cycle)	See Case Setup	[P-intake-avg]
Cylinder Number for Pressure Phasing and EGR Comp.		def (=1)
Pressure Flag		intake
Backflow Heat Transfer Multiplier		def (=0)
Time-Averaged Temperature	See Case Setup	[T-intake-avg]
Composition (Fresh Charge)		air
EGR Fraction (Intake)	fraction	0

Attribute	Unit	Object Value
Instantaneous Pressure		P-exhaust-inst
Crank Angle Array for Multi Cycle Data	deg	ign
Time-Averaged Pressure/Pressure Shift (Multi Cycle)	See Case Setup	[P-exhaust-avg]
Cylinder Number for Pressure Phasing and EGR Comp.		def (=1)
Pressure Flag		exhaust
Time-Averaged Temperature	See Case Setup	[T-exhaust-avg]
Composition (Fresh Charge)		air
EGR Fraction (Intake)	fraction	def (=0)

Figure 42: Specifics of the extreme blocks of the Three Pressure Analysis, representing the boundary conditions

Above the portion of the complete model including the block seen several times throughout this thesis, a macro-block can be noticed. It is a standard block included in the library of the software to account for the friction related to the valve lift. A zoom-in of the block and its links with the model is provided by Figure 43. Some blocks of the model for this figure were removed for better highlighting the links between the control block and the model.

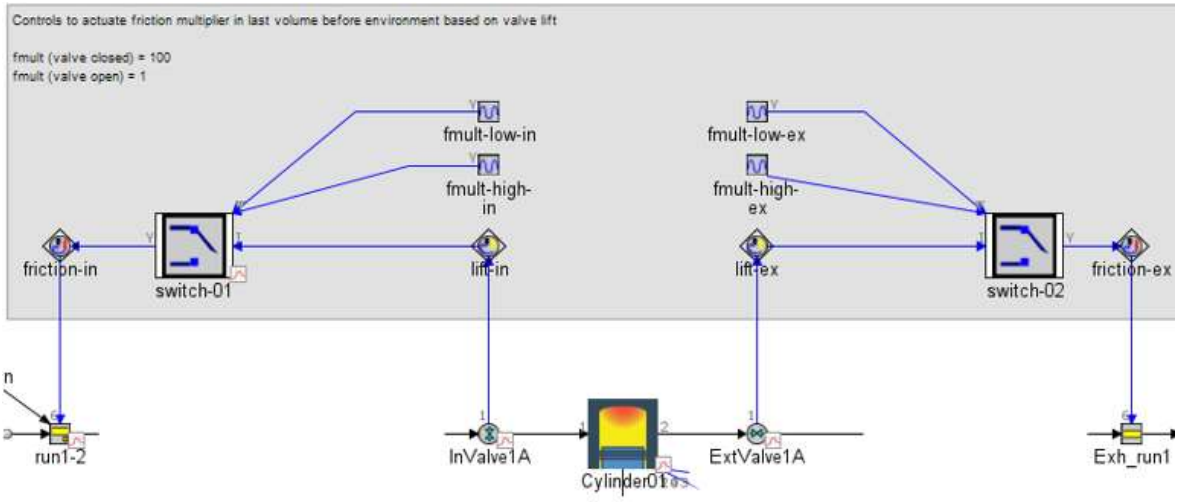

Figure 43: zoom in of the controls for the imposition of the friction multiplier

Inside the cylinder, the focus for what the setup is concerned is inside the *Measured Cylinder Pressure Analysis Object* (Figure 44).

Main Output

	Attribute	Unit	Object Value
	Measured Data Object		PressureCycle ...
◉	Target Combustion Efficiency		
○	Target Unburned Fuel Concentration		
	Start of Burn Rate	See Case Setup	[spark] ...
◉	Automatic End of Measured Burn Rate		SI
○	Imposed End of Measured Burn Rate	deg	def
	End of Analysis		EVO
	Analysis Increment	deg	def ...
	Number of Temperature Zones		single-temp
	Entrained Fuel-Air Option		homogeneous
	Combustion Object for Forward Run		def ...
	Knock Analysis Object		ign ...

Figure 44: Focus on the setup of the cylinder in the TPA

In particular, the pressure cycle relative to the ensemble average of the measured pressure cycles should be inserted. Subsequently, the start of burn rate should be specified. Being this a spark-ignition engine, that coincides with the spark. Analogously, the end of the analysis must be set and – in this case – it is forced to the Exhaust Valve Opening (EVO). Here, the single-temperature zone was set, since there was no point of accounting separately for the burnt gas and the unburnt gas. An important setting to be pointed out is the employment of the hypothesis homogeneous charge. This is a typical operation that is accomplished during the phase of calibration of a predictive model. In other words, this option considers the charge to be homogeneous and at a specific air-to-fuel ratio, imposed through the injector, as discussed in the previous chapter about the imposed-combustion model. Additionally, the "Flow Object" had to be filled with the necessary parameters, i.e. the geometrical information about the piston cup and – more important – the three multipliers that are the object of the optimization.

Attribute	Object Value
Turbulence	
Production Term Multiplier	[ProdTermMult] ...
Geometric Length Scale Multiplier	[LengthScaleMult] ...
Intake Term Multiplier	[IntakeMult] ...
Spray/Jet Term Multiplier	0 ...

Figure 45: Setup of the parameters object of optimization

From Figure 45, the parameters that will undergo the optimization are presented:

- Production term multiplier: governing the production of turbulence from the mean flow, thus directly acting on the TKE
- Geometric Length Scale multiplier: governing the length scale at which turbulence and dissipation processes occur. In other words, the higher this parameter, the higher the produced level of turbulence
- Intake term multiplier: governing the contribution of intake flow through valves to mean kinetic energy.

No Spray/Jet multiplier is considered, since the engine layout does not foresee a pre-chamber.

Regarding the operative point of view, an additional subsystem was included in the TPA model (Figure 46).

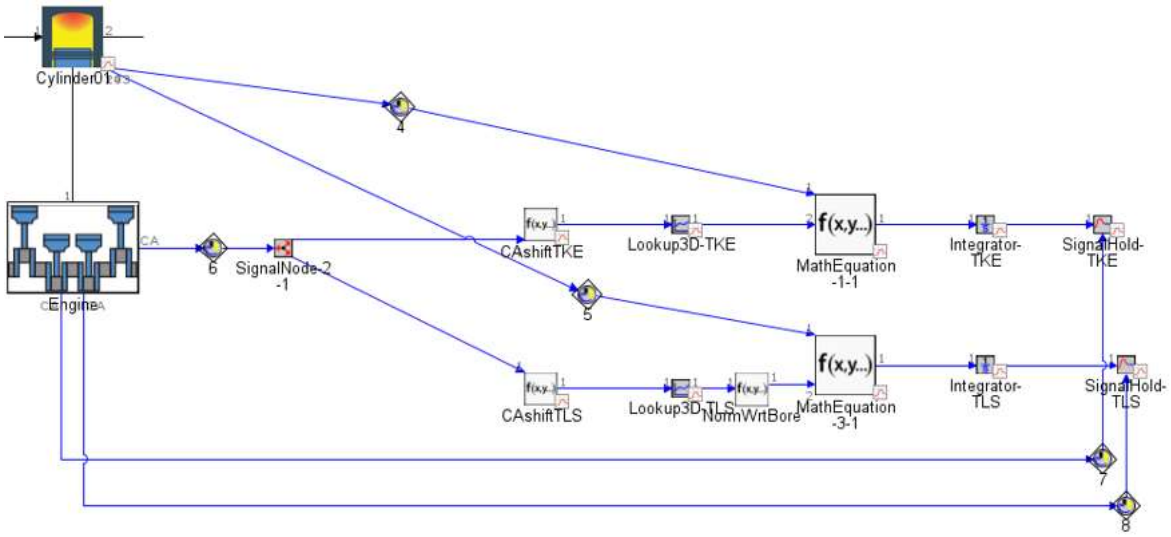

Figure 46: layout of the blocks that compute the objective function for the optimization of the TPA

This element has the scope of first computing of the error of the TKE and of the TLS, relative to the results provided by the 3D-CFD analysis. As clear from the figure, the subsystem is made of two identical branches, one associated to the TKE, the other to the TLS. Eventually the objective function to be minimized during the optimization is this way available. In particular:

$$Error_{TKE} = \frac{1}{t_{SI} - t_{IVO}} \int_{t_{IVO}}^{t_{SI}} \frac{|TKE_{3D} - TKE_{1D}|}{TKE_{3D}} dt$$

$$Error_{TLS} = \frac{1}{t_{SI} - t_{IVO}} \int_{t_{IVO}}^{t_{SI}} \frac{|TLS_{3D} - TLS_{1D}|}{TLS_{3D}} dt$$

In these formulae, t_{SI} refers to the spark timing, while t_{IVO} indicates the Intake valve opening. Clearly, the integration window is relative to the crank angle window within which the turbulent phenomena are of interest, so between the start of the flow towards the cylinder and the ignition. The argument of the integral is contained inside the block *MathEquation*, that receives two external inputs:

- The 1D TKE or TLS directly from the block associated to the cylinder
- The 3D TKE or TLS from a look-up table built through the data received by the 3D-CFD analysis. The crank angle is received from the crank train and then shifted from the block *CAshift*, created on purpose to align the crank angle range employed in the 3D analysis and the crank angle range 0 ÷ 720 °CA employed by GT-SUITE.

Methodologically speaking, a paramount importance is covered by the block *SignalHold*.

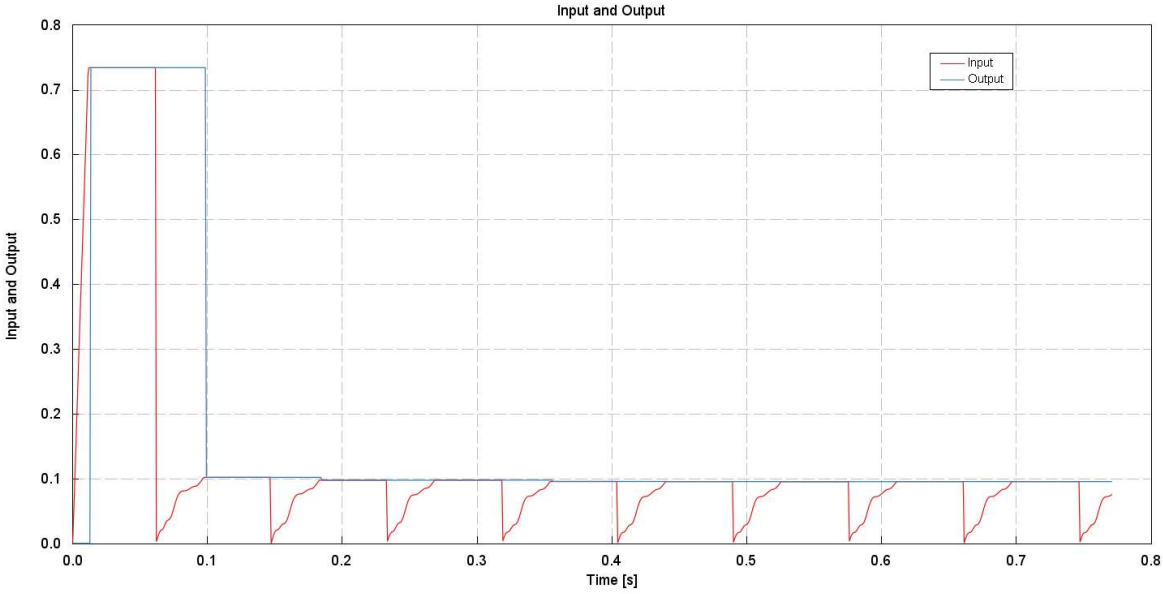

Figure 47: Effect of the employment of the block Signal Hold in the objective function

As visible from Figure 47, the output of the integrator along time is not constant, and the error close to the spark is the needed quantity. Since this latter is the last value that is obtained during the integration, it is possible to make the output of the integrator the ensemble of the actual errors integrated along time, therefore the objective function will be a smoother signal.

At this point, the optimizer had to be set. Figure 48 provides the overview of the setup of this tool.

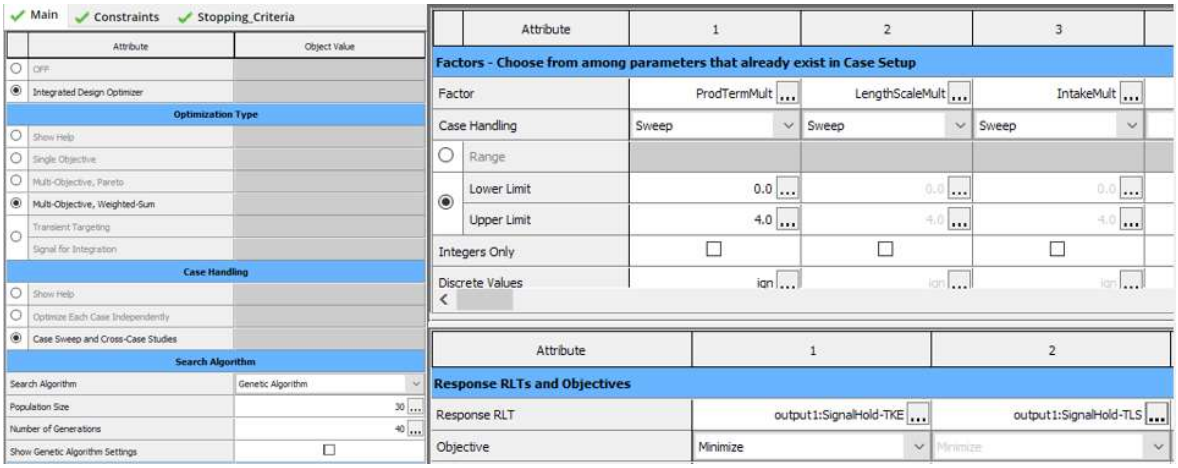

Figure 48: Layout of the optimizer

The rough idea beyond this phase was to reach can be at a first glance summarised with the following points:

- Full convergence of each objective function
- Optimum value of each parameter not corresponding to an extreme value of the designed range
- Optimization of each parameter that takes into account the influence of the other parameters on the minimization of the objective function

For this purpose, the Genetic Algorithm was. Basing on the guidelines of GT-SUITE, 40 generations were decided to be considered for each member of the population. In fact, this number is about three times the value suggested as default by GT-SUITE; this was made in order to be sure not to exclude any possible design. A similar rationale was followed for the population size. For an optimization with 3 factors, GT-SUITE suggests a size of 10, however it was set to 30, so to ensure the full convergence. The expected value of each parameter was in the order of 0.5 ÷ 1, however, to fulfil the second point of the above list, the range 0 ÷ 4 was decided for the sweep of each factor (with a step of 0.1).

In terms of results, two regimes were considered: 1400 rpm and 2400 rpm, i.e., the regimes that were analysed in the 3D analysis and for which the look-up tables were available. Various optimizations were made: the area of interest for this purpose is the crank angle range close to the spark timing; the lower the integration window, the better the trend in that area. Nevertheless, having a wide integration window is necessary in order to obtain good predictive capabilities. Basing on the obtained results, a trade-off between these two aspects must be found.

Among the various combinations of parameters that were considered following the above-mentioned rationale, the optimization presented in Figure 49 and Figure 50 showed the best compromise in terms of behaviour close to the spark and predictive capabilities, for the two considered regimes.

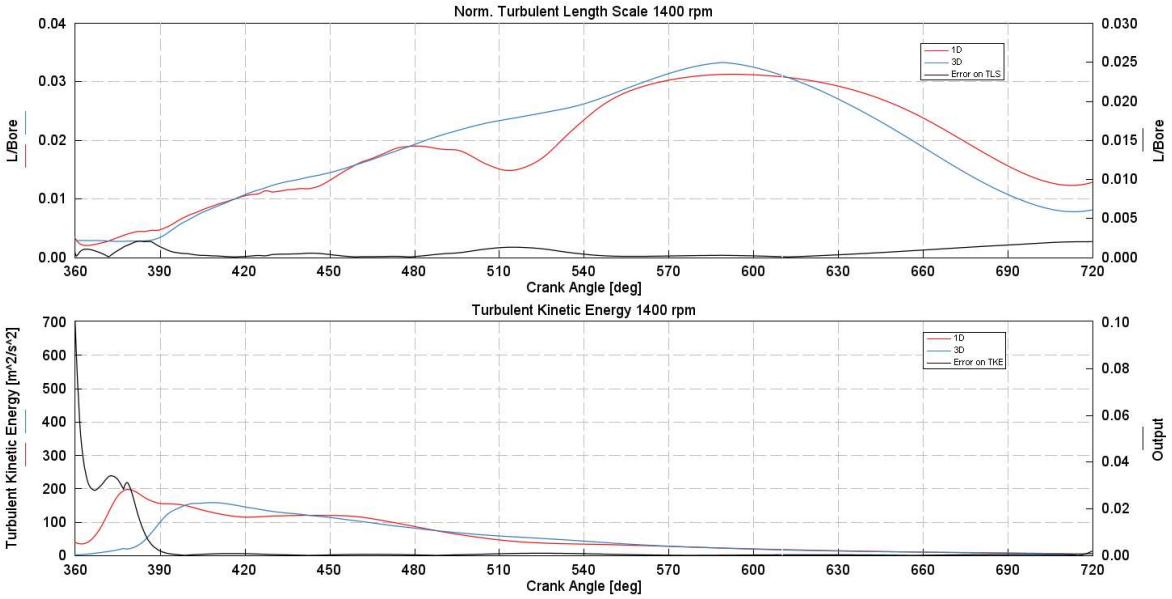

Figure 49: Results obtained for the Turbulent Length Scale (above) and the Turbulent Kinetic Energy (below), at 1400 rpm

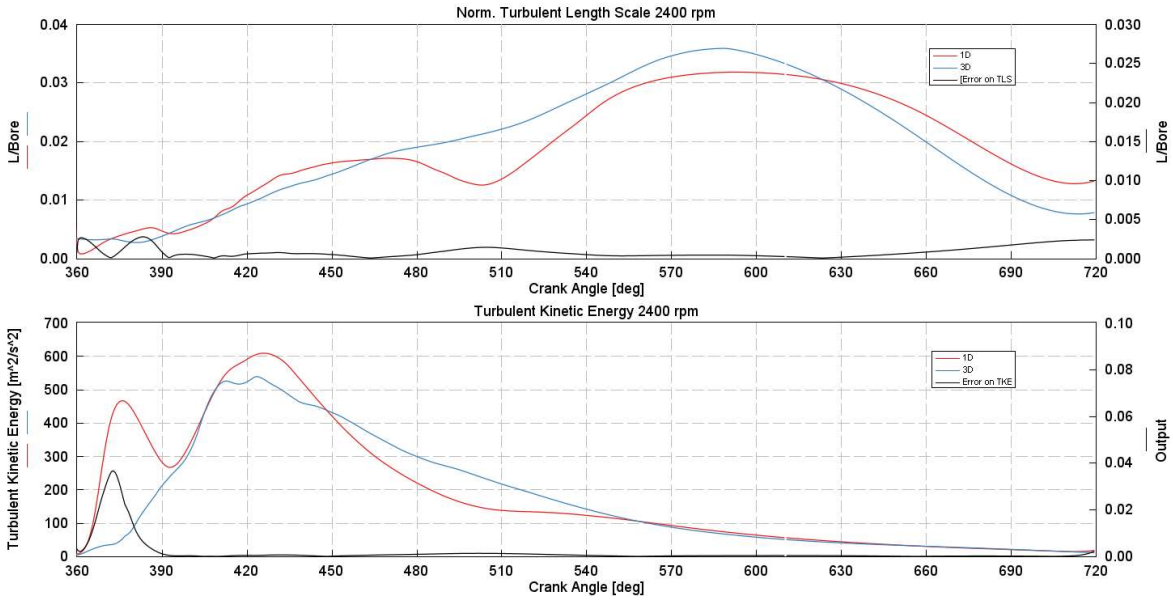

Figure 50: Results obtained for the Turbulent Length Scale (above) and the Turbulent Kinetic Energy (below), at 2400 rpm

The considered crank angle window is of 300 °CA. For the two regimes under analysis, t_{SI} and t_{IVO} are necessarily different, however the integration range is the quantity of interest

for this analysis. As a remark, the normalization of the TLS with respect to the cylinder bore is a usual operation that is done and suggested in the case RLT of GT-SUITE as well. From the graphs, it is clear how the 0D/1D-CFD model resembles solidly the traces of the two examined quantities for both the regimes, up to matching punctually the TKE during the second half of the compression stroke. On its side, the TLS presents an error close to zero throughout the cycle and in correspondence of the spark. For sake of completeness, Figure 51, Figure 52 and Figure 53 show the optimizations of the three multipliers of interest. As visible, each trace fulfils the requirements that were enlisted previously.

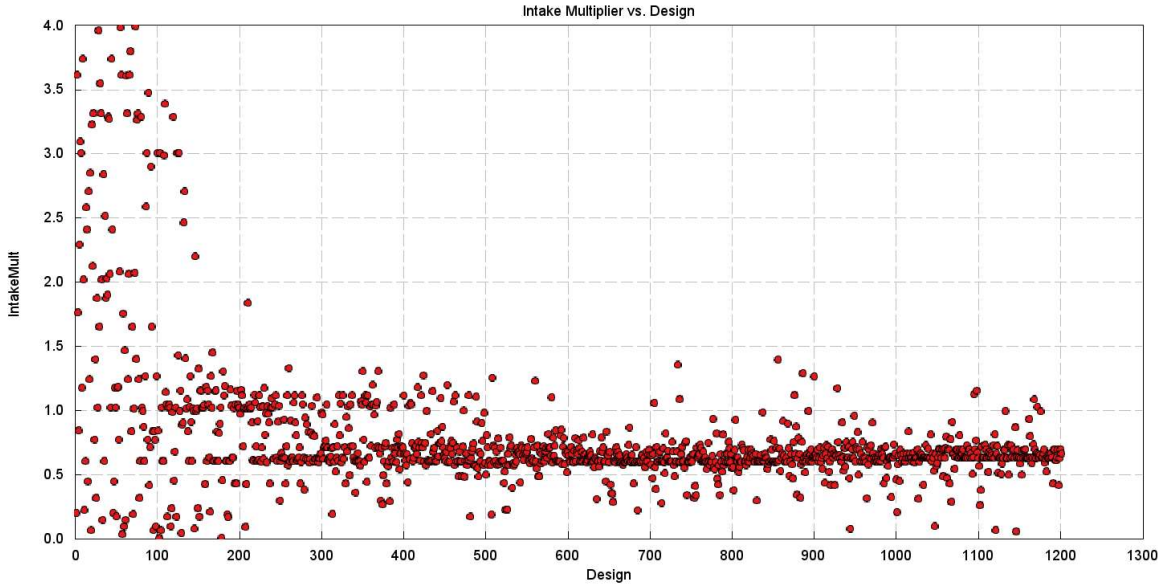

Figure 51: Trace of the designs accomplished by the optimizer for the Intake multiplier

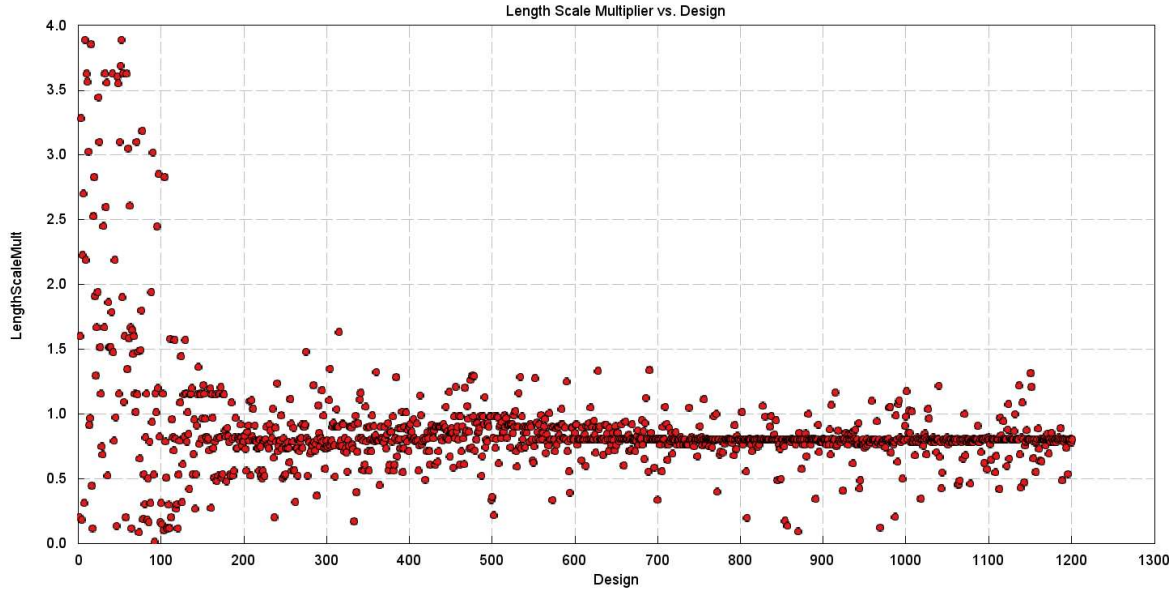

Figure 52: Trace of the designs accomplished by the optimizer for the Length Scale multiplier

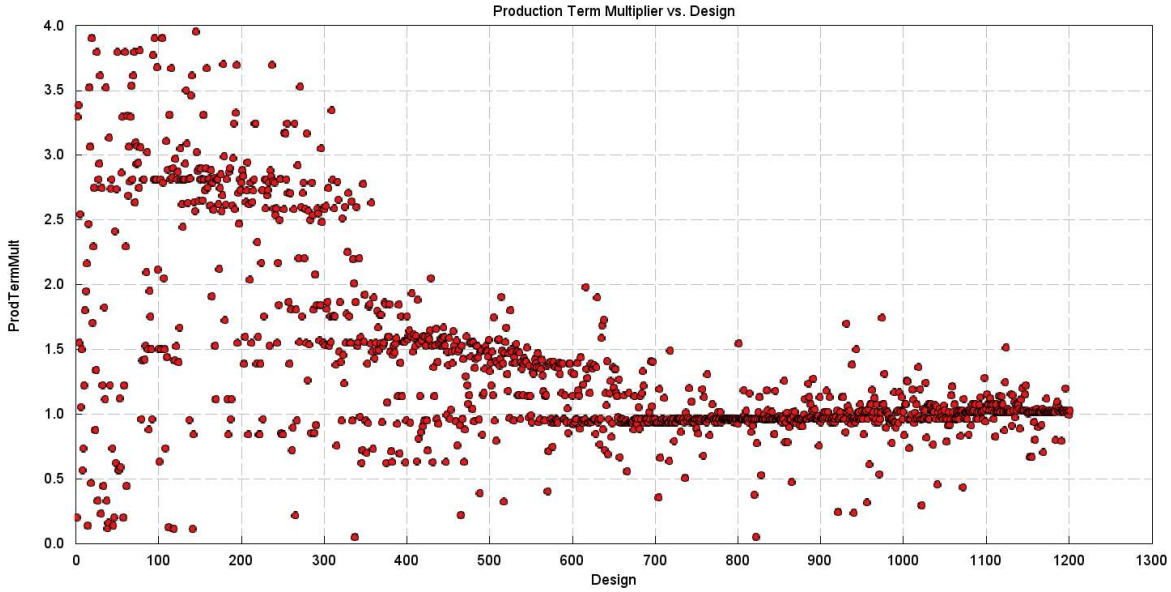

Figure 53: Trace of the designs accomplished by the optimizer for the Production Term multiplier

Table 3 Shows the optimal values for the three multipliers.

Multiplier	Value
Intake multiplier	0.6637
Production Term multiplier	10.258
Length Scale multiplier	0.8008

Table 3: Values of the multipliers retrieved from the optimization

The obtained results are overall satisfactory and pave the way for the setup of the second part of the calibration of the predictive model, i.e., the CPOA.

5.3 The CPOA with predictive model

The following step is assessed in a CPOA environment to account for the fact that an operation with no gas exchange is considered. This type of analysis is called "*M+P*", meaning "measured and predicted". In other words, the results will be not only those of a basic CPOA, but also the predicted quantity will be plotted in the output file. Before passing to the selection of the calibration dataset, the main aspect regards the setup of the SITurb model; however, a crucial preliminary adjustment must be done. Figure 54 shows the tab *Initialization/Imposed* of the *Flow Object*.

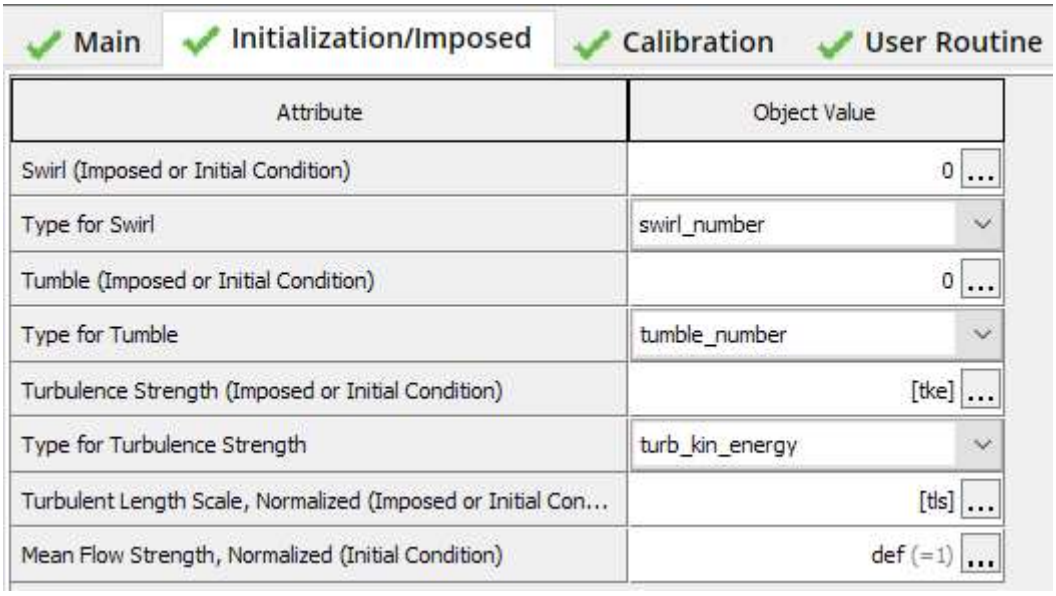

Figure 54: Setup of the turbulence parameters inside the cylinder for the CPOA analysis

From the run of the optimized Three Pressure Analysis that was discussed in the previous paragraph, the case RLT provides the arrays of values to be put for each case of the CPOA. The relevant parameters in terms of turbulence must be inserted in this tab, in order to include the results obtained from the previous analysis. An analogous operation has to be accomplished in the tab *Calibration*, in which the cases relative to the Production Term Multiplier, the Geometric Length Scale Multiplier and the Intake Term Multiplier found in the optimization must be fulfilled.

This completed, the setup for the calibration of the SITurb can be finally started. This model is contained in the section *Combustion Object*. The tab *Main* requires the so-called *Flame Geometry Object*. In addition to the initial dimension of the spark and the array of the spark timing, the *Flame Geometry Object* must be set (Figure 55).

Main | LamSpeed | TrbSpeed | Advanced | Startup

	Attribute	Unit	Object Value
	Model Version		v2016
	Flame Geometry Object		SparkLocation ...
	Combustion Anchoring Option		SparkTiming
	Spark Timing or Anchor Angle	deg	=-[SA(deg)] ...
	Initial Spark Size	mm	1 ...
☐	Asynchronous Flames: Spark Timing Separation	deg	
☐	Stratification: Entrained Mixture Equivalence Ratio Profile		

Figure 55: Setup of the main of the SITurb model

The spark location was fulfilled thanks to the parallel 3D-CFD analysis; the head and valve geometry was set by direct measurements on the CAD. Eventually, the CAD of the piston was loaded in the tab *Piston Geometry* and then oriented through the direction cosines; coherently with the CAD, the piston axis was directed along the vertical axis (Figure 56).

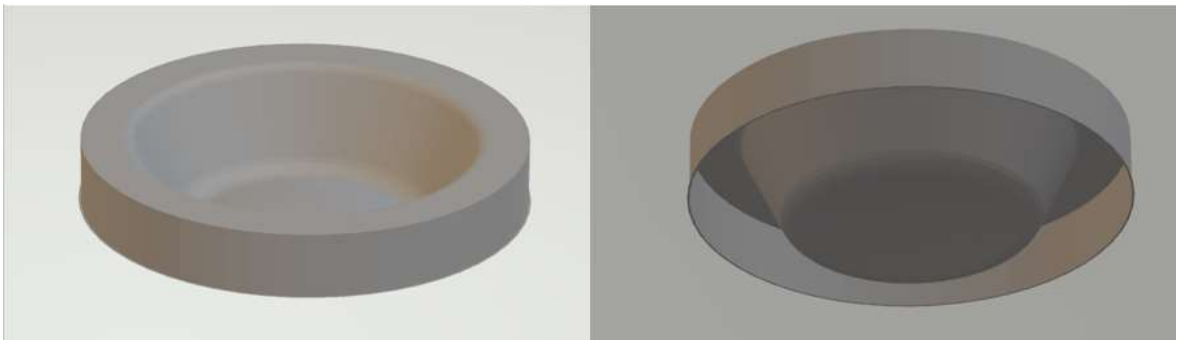

Figure 56: CAD of the piston employed for the setup of the SITurb model

The tabs *LamSpeed* and *TrbSpeed* are the other tabs of interest. They deal with the employed fuel and the parameters that will be object of calibration. In *LamSpeed*, hydrogen was set as fuel, and the dilution multiplier was created (Figure 57).

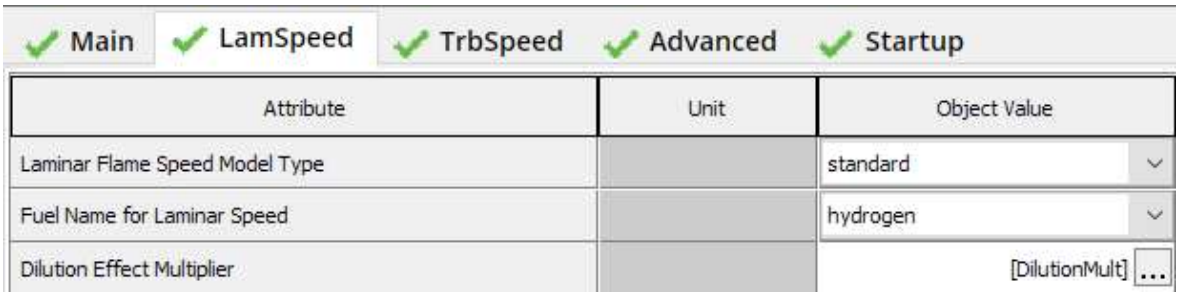

Figure 57: setup of the quantities influencing the laminar speed of the flame front inside the SITurb model

That of dilution is a crucial parameter since the presence of any dilutant agent (EGR, air, residuals, etc.) slows down the laminar flame speed. The relationship between the laminar flame speed S_L and the Dilution Effect Multiplier (DEM) considered by GT-SUITE is

$$S_L = \left(B_m + B_\phi(\phi - \phi_m)^2\right)\left(\frac{T_u}{T_{ref}}\right)^\alpha \left(\frac{P}{P_{ref}}\right)^\beta f(Dilution)$$

where

$$f(Dilution) = 1 - 0.75 * DEM(1 - (1 - 0.75 * DEM * Dilution)^7)$$

In the formulae:

- B_m is the Maximum Laminar Speed
- B_ϕ is the Laminar Speed Roll-off Value

And they are specific of the chemical species of the fuel

- ϕ is the equivalence ratio
- ϕ_m is the equivalence ratio at maximum speed (specific for hydrogen)
- P, T are the (computed) pressure and temperature
- P_{ref}, T_{ref} are the pressure and temperature at the reference conditions (101325 Pa, 298 K)
- T_u is the temperature of the unburned gas
- $Dilution$ is the mass fraction of residuals in the unburned gas
- α, β are respectively the temperature and pressure exponent (specific for hydrogen)
- $f(Dilution)$ is the dilution effect
- DEM is the Dilution Effect Multiplier (object of optimization)

In *TrbSpeed* the other multipliers relative to the flame speed subject to turbulence are set:

- Flame Kernel Growth Multiplier: governing the ignition capability, or better, the higher this multiplier, the lower the ignition delay
- Turbulent Flame Speed Multiplier: scaling the turbulent flame speed proportionally, and so the combustion duration
- Taylor Length Scale Multiplier: acting on the time constant of combustion of fuel/air mixture entrained into the flame zone by changing the thickness of the plume

For the choice of the calibration dataset, a first check was of duty in terms of the swept main calibration parameters, i.e., air-to-fuel-ratio, rotational speed, spark timing, boost pressure). In this sense, many cases presented a cycle with absent or extremely retarded combustion (Figure 58 and Figure 59 can be used as a support) and were performed by the company for the analysis of some aspects that lie outside of the scope of this thesis, therefore they were checked and excluded from the considered dataset for both the calibration and the validation. This way, about 170 cases resulted to be suitable for this analysis – out of the nearly 260 provided cases – and 45 of these were employed to calibrate the combustion model.

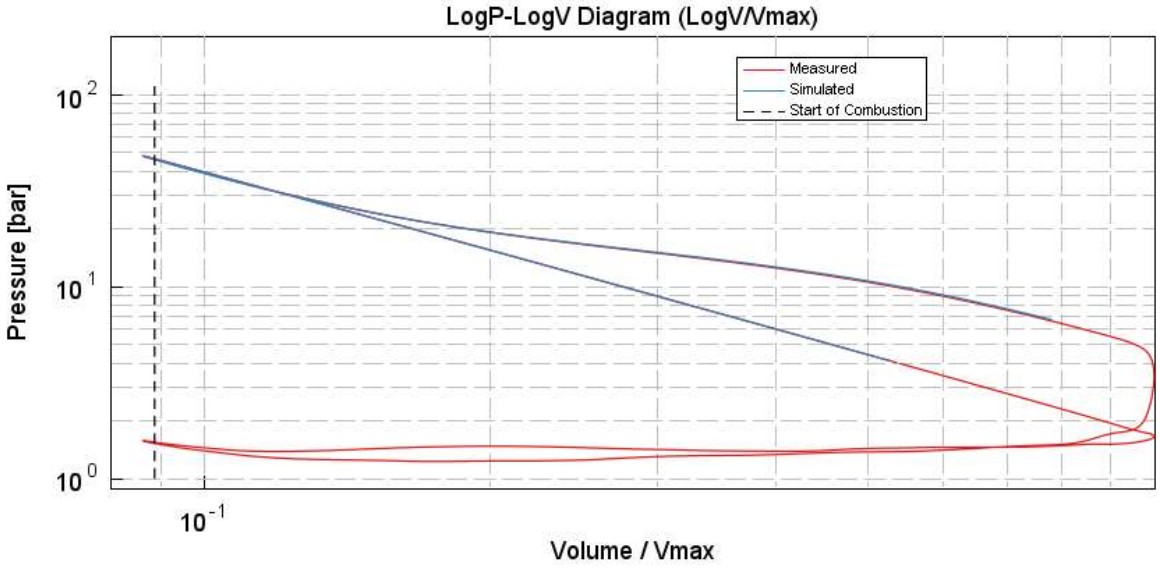

Figure 58: log(p)-log(V) graph of a discarded cycle

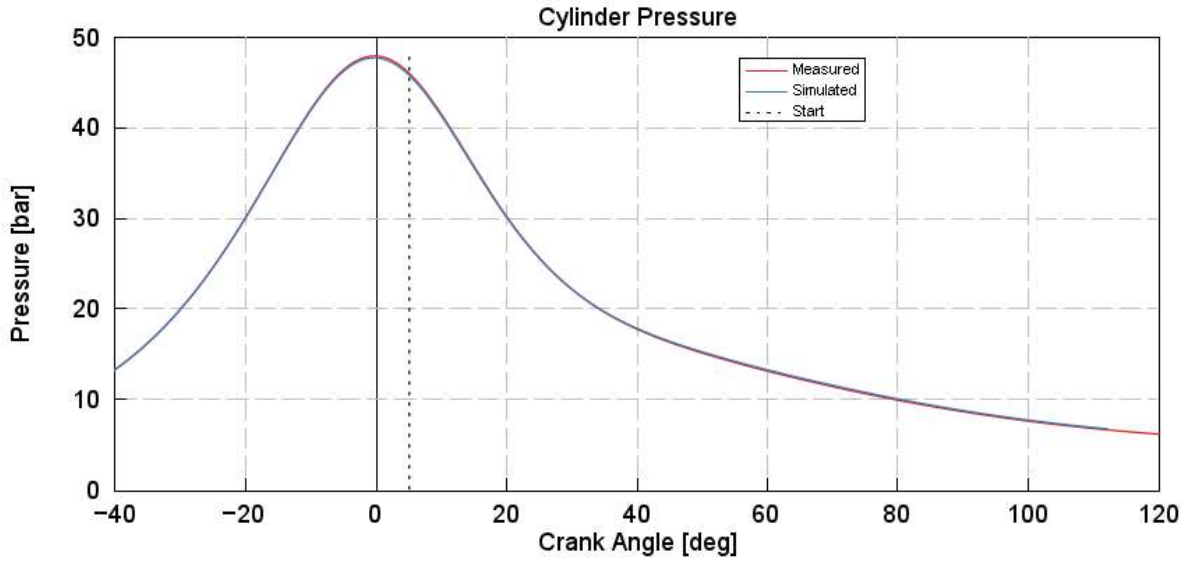

Figure 59: Pressure cycle of an average discarded case

The results obtained with the calibration dataset that was retrieved by following this rationale can be seen in first analysis regarding the comparison between the predicted burn rate and the measured one. Figure 60 can be used as a support.

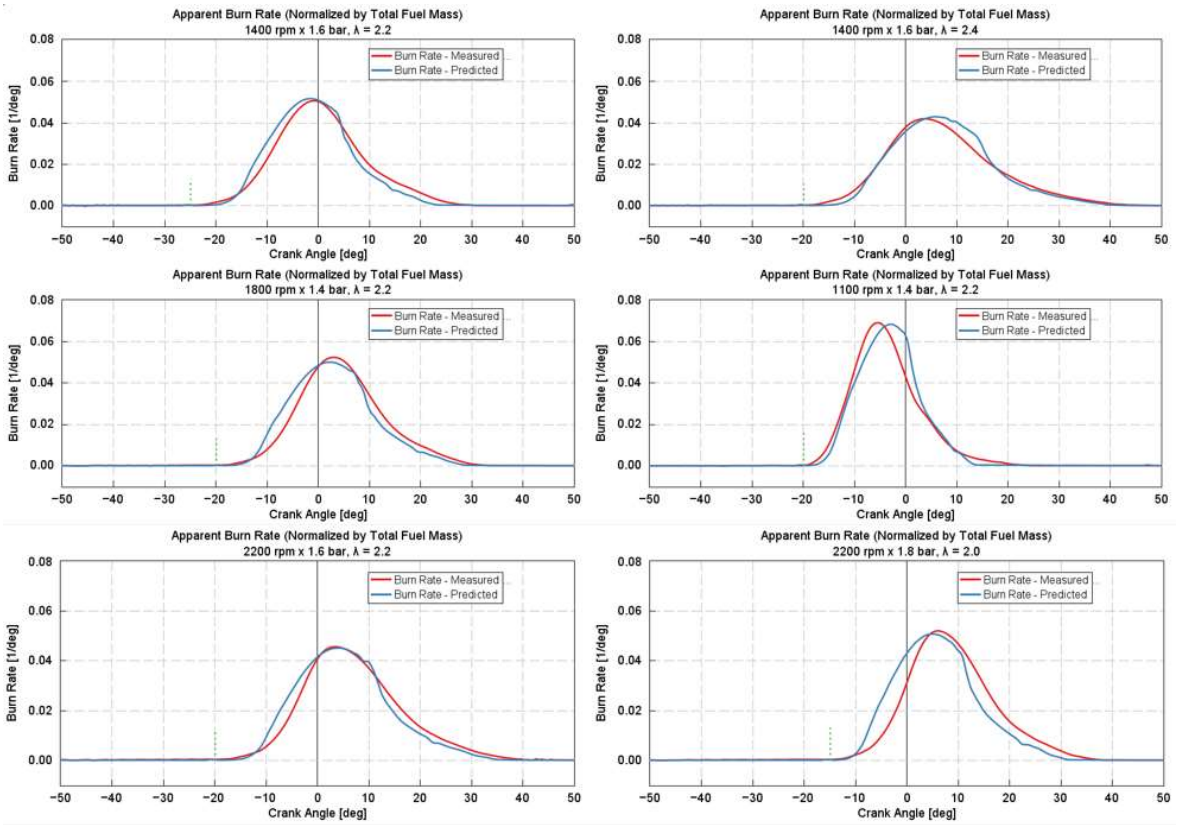

Figure 60: Some explicative obtained burn rates - Measured vs Predicted

The presented graphs can be taken as the most explicative ones, since they include all the speed regimes and the most employed boost pressure and air-to-fuel ratios. As clear from the graphs of Figure 60, the burn rate traces obtained by the calibration well resemble the experimental burn rates. As anticipated several times previously, the point of the calibration is providing a forecast of the trends of the burn rate for each case, not obtaining a punctual prediction. For this calibration, the results are satisfactory, since the shape of the burn rate is well followed by the model and the subtended area by the two curves is visibly equivalent; this translates into the complete burn of the injected fuel also for the predicted cycle. In order to provide a general overview of the whole results of the calibration, some correlation plots in terms of the main characteristics of the combustion process are presented in Figure 61.

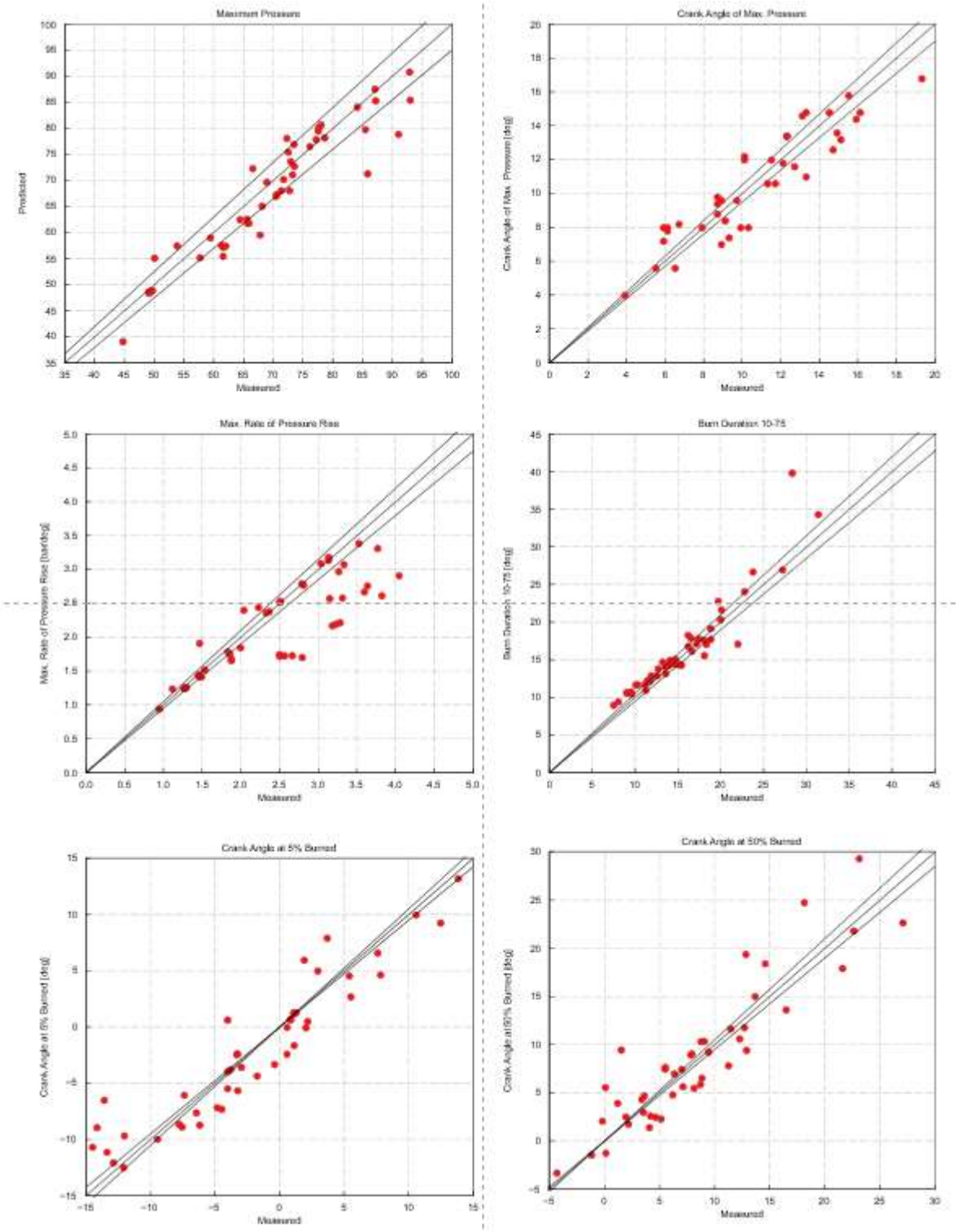

Figure 61: Correlation plots of the results of the calibration of the SITurb model

Dealing with the maximum pressure, the results are solid and suggest a good performance with respect to the reaching of the IMEP target (this aspect is additionally dealt later on the paragraph). In terms of maximum rate of pressure rise, the correlation is good and although

the 5% margin is overcome, the absolute error is not of concern. The burn duration 10%-75% was chosen to leave the very beginning and the last part of the combustion process out of this analysis, in order to focus on the development of the actual core of the flame front. Under this point of view, the calibration is solid. Passing to the MFB5 and the MFB50, the error margin is not respected, however the trend resembles the experimental data, and the absolute error is acceptable (in the order of 2 Crank Angle Degrees).

In general, as clear from the graphs included in the figure, the prediction is not punctual and most of the points lay out of the 5% error margin. However, the results of this calibration come from an analysis in which the calibration dataset considers quite a large variety of condition that is as heterogeneous as possible with respect to four swept parameters (engine speed, air-to-fuel ratio, spark timing, boost pressure) in order to give the best possible predictive capabilities to the model.

Subsequently, the analysis was extended to the whole validation dataset – i.e., the remaining cases of the whole provided experimental data. The obtained results can be in first analysis presented with respect to the same quantities as in the calibration procedure (Figure 62), then in Table 4 the results are presented quantitatively.

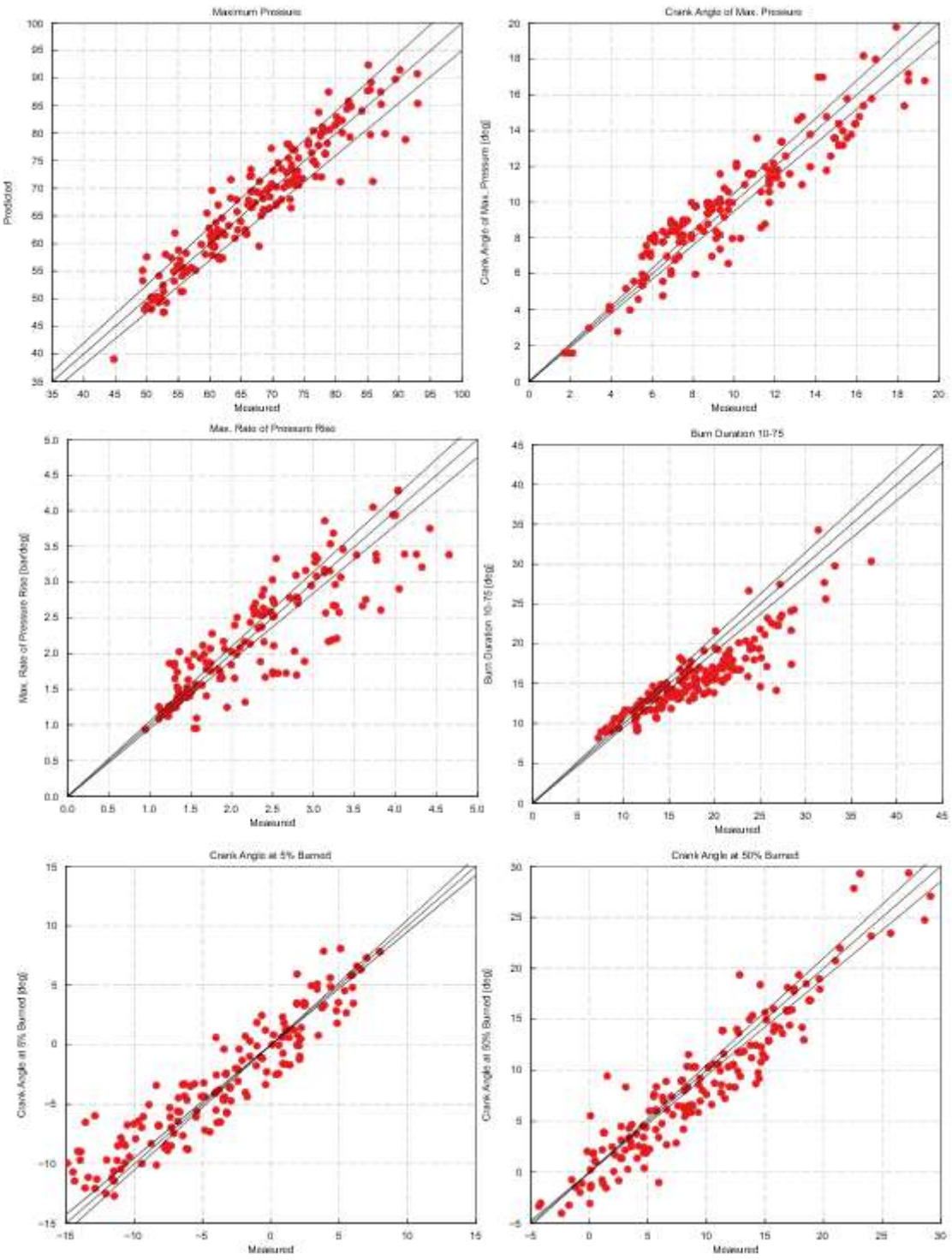

Figure 62: Correlation plots of the results of the validation of the SITurb model

Quantity	RMS error
Maximum pressure [bar]	3.76
Crank angle of maximum pressure [deg]	1.38
Maximum rate of pressure rise [bar/deg]	0.42
Duration 10%-75% [deg]	3.40
Crank angle of 5% burned mass [deg]	2.26
Crank angle of 50% burned mass [deg]	2.77

Table 4: Root Mean Square error measured for the relevant quantities of the combustion process, after the validation of the SITurb model

With respect to the whole dataset, the RMS errors calculated above show the validity of the SITurb model. To support this statement, some comparison with respect to the main quantities can be presented. It is possible to relate to Figure 63, Figure 64 and Figure 65; for sake of clarity, only two representative values of lambda will be presented, at the regime of 1400 rpm, 1.6 bar boost. The choice of the shown air-to-fuel ratio is such to provide an overview of what happens also in case of extremely lean operations, in order to present also the less solid aspects, in perspective of future development as well.

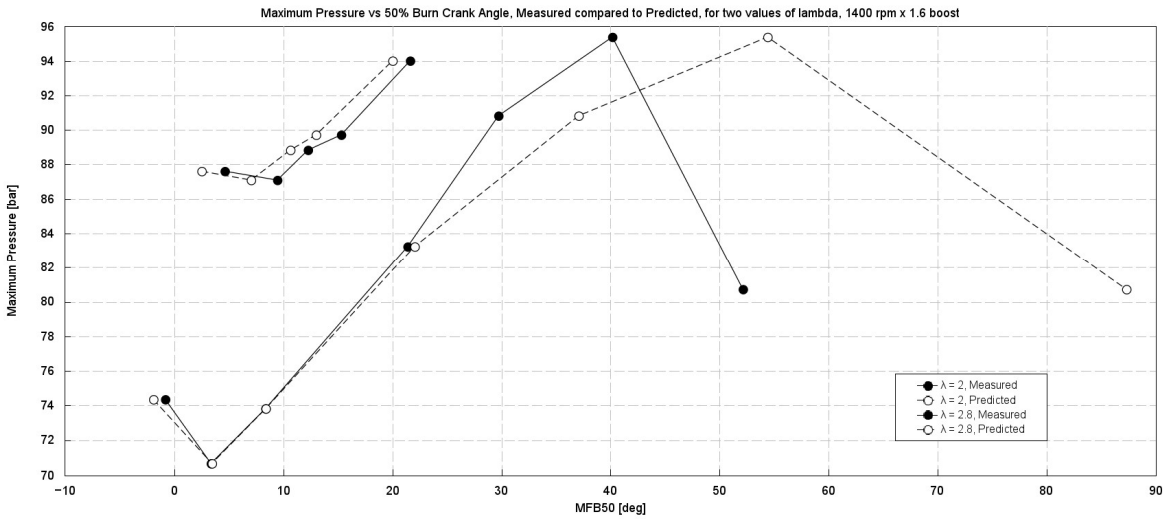

Figure 63: Comparison for λ = 2 and λ = 2.8 for the maximum in-cylinder pressure, Measured vs Predicted, for a sweep of MFB50

Figure 63 shows in a clearer way what was say previously. In terms of maximum pressure, the model results to be solid, dealing with both trends against MFB50 and quantitatively. The predictive capabilities loose quality when dealing with retarded or slow combustion processes, especially when considering particularly lean operative conditions.

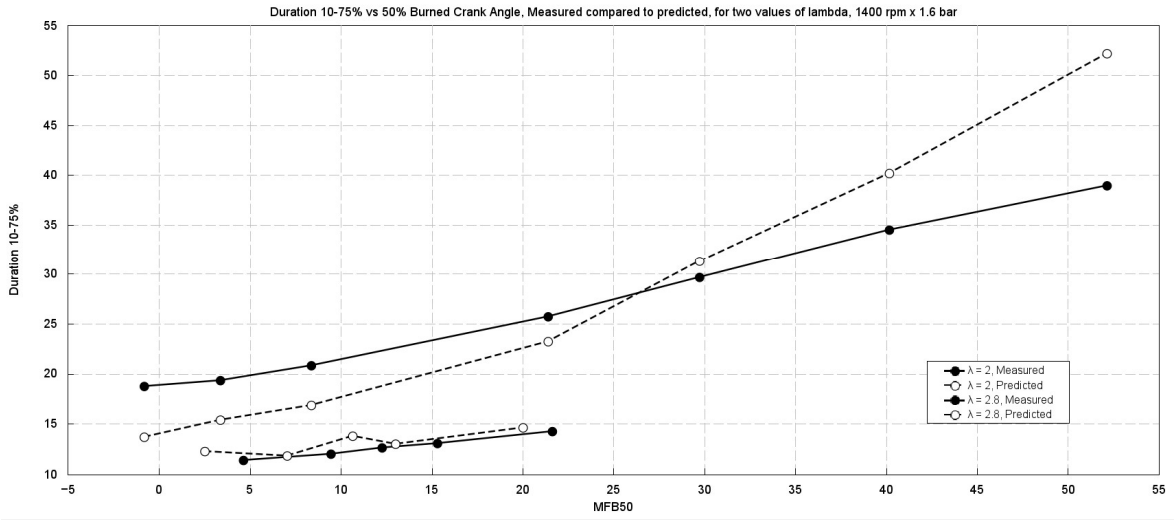

Figure 64: Comparison for λ = 2 and λ = 2.8 for the 10-75% duration of combustion, Measured vs Predicted, for a sweep of MFB50

Figure 64 resembles what expressed for Figure 63, in terms of 10-75% duration. Again, the core of the combustion duration is promisingly followed by the predictive model, even in case of extremely lean operations. This gives added value to the developed SITurb model.

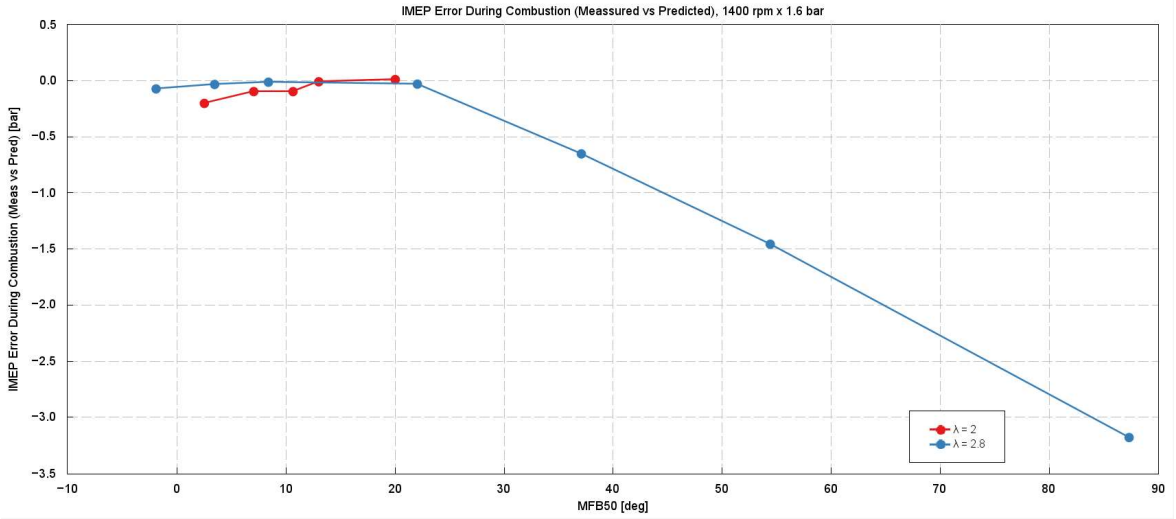

Figure 65: IMEP Error of the Predictive model with respect to the experimental data, for λ = 2 and λ = 2.8

Figure 65 aims to present the difference in IMEP between the predictive model and the experimental data. The relevant aspect of this diagram is the fact that not only the difference in this fundamental performance approaches zero when considering relatively rich mixtures, but also, a good matching (within 1 bar of absolute error) is reached for combustion processes characterised by a 50% mass fraction burned crank angle up to 40 degrees after TDCf, thus giving additional credit to the results of the validation of the SITurb model.

6. Conclusions and future developments

The following thesis aimed at providing the basis for the development of a 0D/1D-CFD predictive model for a turbocharged 3.5 L PFI engine fuelled with hydrogen, installed at the test bench of Westport Fuel Systems in Cherasco (TO). The foreseen employment of this engine is in the Heavy-Duty Vehicles sector, for the abatement of the CO_2 emissions and the ecological transition for the transports sector. Starting from the provided experimental data and the geometrical information of the engine, an imposed-combustion model was developed from scratch employing GT-SUITE and its tools. Once the imposed-combustion model was solidly correlated to its real counterpart, the predictive SITurb model was developed, first optimizing the parameters influencing the turbulent flow entering the cylinder, then calibrating and validating the combustion model, basing on the experimental dataset provided by the company. The results of the validation procedure showed the high potential of this model in predicting the majority of the considered operating conditions, despite a remarkable portion of the provided experimental dataset resulted to be unemployable for this scope. The correlation resulted to partially loose some validity when dealing with extremely lean operating conditions and/or slow or retarded combustion. Therefore, as possible future development, an enhanced calibration and validation of the SITurb model could be assessed, in terms of quantity of employable operating conditions. Therefore, the implementation of the obtained SITurb in the complete 0D/1D-CFD model and the consequent correlation with the experimental results could be assessed. This way, the obtained results could represent a strong tool for increasing the efficiency of the operations at the test bench, in terms of time and economics.

Bibliography and references

[1] F. Millo, Engine Emissions Control, Politecnico di Torino, 2023-2024.

[2] S. D'ambrosio, Propulsion Systems and Their Applications to Vehicles, Politecnico di Torino, 2024-2025.

[3] C. Novara, Driver Assistance Systems Design - Part A, Politecnico di Torino, 2025-2025.

[4] A. Piano, F. Pucillo, F. Millo, S.Giordana, N. Rapetto, C. Schuette, "Experimental investigation on the optimal injection and combustion phasing for a direct injection hydrogen-fuelled internal combustion engine," *Elsevier,* 2025. https://doi.org/10.1016/j.ijhydene.2024.12.194

[5] A. Piano, G. Quattrone, F. Millo, F. Pesce, A. Vassallo "Development and validation of a predictive combustion model for hydrogen-fuelled internal combustion engines," *Elsevier,* 2024. https://doi.org/10.1016/j.ijhydene.2024.09.407

[6] N. Fogla, "Development of a K-k-epsilon Phenomenological Model to predict in-cylinder turbulence," *ResearchGate,* 2017. DOI: 10.4271/2017-01-0542

[7] International Energy Agency, "Global Hydrogen review," Paris, 2024. https://www.iea.org/reports/global-hydrogen-review-2024

[8] S. Verhelst, T. Wallner "Hydrogen-Fueled Internal Combustion Engines," Progress in Energy and Combustion Science, 2009. https://doi.org/10.1016/j.pecs.2009.08.001

[9] C. M. White, R. R. Steeper, A. E. Lutz, "The Hydrogen-Fueled Internal Combustion Engine: A Technical Review", International Journal of Hydrogen Energy, 2006. https://doi.org/10.1016/j.ijhydene.2005.12.001

[10] L. M. Das, "Hydrogen Engines: A View of the Past and a Look into the Future", International Journal of Hydrogen Energy, 1990. https://doi.org/10.1016/0360-3199(90)90200-I

[11] C. Cunanan et al., "Heavy-Duty Vehicle Powertrain Technologies: Diesel, Battery Electric and Hydrogen Fuel Cells — A Review", Clean Technologies, 2021. https://doi.org/10.3390/cleantechnol3020028

[12] S. E. Hosseini, B. Butler, "An Overview of Development and Challenges in Hydrogen-Powered Vehicles", International Journal of Green Energy, 2020. https://doi.org/10.1080/15435075.2019.1685999

[13] F. Ueckerdt et al.,"Potential and Risks of Hydrogen-Based E-Fuels in Climate-Change Mitigation", Nature Climate Change, 2021. https://doi.org/10.1038/s41558-021-01032-7

[14] J. M. M. Arcos, D. M. F. Santos, "The Hydrogen Colour Spectrum: Techno-Economic Analysis of Production Pathways", Gases, 2023. https://doi.org/10.3390/gases3010002

[15] Hydrogen Europe, "Long-Term Outlook on Zero-Emission Mobility", Technical Report, 2024. https://hydrogeneurope.eu/wp-content/uploads/2024/02/2024.02.14-Long-term-outlook-on-zero-emission-mobility_Report_14-02-2024_DIGITAL.pdf

[16] Hydrogen Council, "Hydrogen Scaling Up: A Sustainable Pathway for the Global Energy Transition", Technical Report, 2017. https://hydrogencouncil.com/en/study-hydrogen-scaling-up

[17] Gamma Technologies, https://gtisoft.com/gt-suite/

[18] Gamma Technologies, “GT-ISE Help, Reference Manual”, 2022.